Dispersion-dissipation analysis of 3D continuous and discontinuous spectral element methods for the elastodynamics equation

A. Ferroni[1], P.F. Antonietti[1], I. Mazzieri[1], A. Quarteroni[2,1(on leave)]

[1] *MOX– Laboratory for Modelling and Scientific Computing, Department of Mathematics,*

Politecnico di Milano, Piazza L. da Vinci 32, 20133 Milano, Italy

alberto.ferroni@polimi.it,paola.antonietti@polimi.it,ilario.mazzieri@.polimi.it

[2] *Chair of Modeling and Scientific Computing (CMCS),*

Mathematics Institute of Computational Science and Engineering (MATHICSE),

École Polytechnique Fédérale de Lausanne (EPFL), Station 8, 1015 Lausanne, Switzerland.

alfio.quarteroni@epfl.ch

SUMMARY

In this paper we present a three dimensional dispersion and dissipation analysis for both the semi discrete and the fully discrete approximation of the elastodynamics equation based on the plane wave method. For space discretization we compare different approximation strategies, namely the continuous and the discontinuous spectral element method on both tetrahedral and hexahedral elements. For time discretization we employ a leap-frog time integration scheme. Several numerical results are presented and discussed.

Key words: Continuous and Discontinuous Galerkin spectral element methods – Tetrahedral and hexahedral elements – Elastodynamics equation – Dispersion-dissipation analysis.

1 INTRODUCTION

In the field of computational seismology the use of accurate and efficient numerical methods is essential for the study of wave propagation phenomena in complex and heterogeneous media. Most representative numerical schemes applied to seismic wave propagations, rupture dynamics and earthquake ground motion can be divided into the finite-difference (FD) methods, Fourier pseudo-spectral (FPS) and spectral element (SE) methods. In this framework, we refer the reader to the books by Moczo et al. (2014) and Fichtner (2010) for an excellent and comprehensive review of all these methods.
The SE method, firstly introduced in fluid dynamics by Patera (1984), is nowadays a well-established technique widely used for the simulations of earthquake dynamics. Pioneering applications of the SE method can be found in (Seriani et al. 1995; Faccioli et al. 1997; Komatitsch & Tromp 1999), while applications of the SE method for 3D local, regional and global scale simulations can be found in Komatitsch & Tromp (2002); Chaljub et al. (2003); Chaljub & Valette (2004); Fichtner et al. (2009); Stupazzini et al. (2009); Chaljub et al. (2010); Peter et al. (2011) , for example.

To handle highly heterogeneous media, e.g. strong contrast in the soil, or in soil-structure interaction problems, flexible techniques such as the discontinuous Galerkin (DG) method (see, e.g., Rivière & Wheeler 2003; Käser & Dumbser 2006), or the discontinuous Galerkin spectral element (DGSE) method (Antonietti et al. 2012, 2016a) have been further developed. The DG approach (both in its high-order or spectral element version) provides accurate solutions and is well suited for parallel implementation. Moreover, the local spatial step and the local polynomial approximation degree can be tailored to the region of interest, according to the mechanical properties or the geometrical features of the computational domain. In such a framework we mention for example a high-order discontinuous approximation combined with an Arbitrary high order DERivatives time integration scheme proposed in Käser & Dumbser (2006); Dumbser & Käser (2006), the spectral discontinuous Galerkin method based on a domain decomposition approach introduced in Antonietti et al. (2012) and the stability analysis provided in Antonietti et al. (2016a,b) for a wide class of DG approximations of the elastodynamics equation. In Antonietti et al. (2012) the discontinuities are imposed only across the macro-regions in which the domain is partitioned, differently for example from (Rivière & Wheeler 2003; Antonietti et al. 2016c,b), where the DG approximation is applied elementwise. For a review of numerical modeling of seismic waves by DGSE methods we refer the reader to Antonietti et al. (2017).

Continuous and discontinuous SE methods are usually based on discretizations made by tensor product elements (i.e., hexahedral elements). However, since generating hexahedral grids for complex geometries may require a huge computational effort, in recent years SE methods have been extended to triangular and tetrahedral grids (see, e.g., Karniadakis & Sherwin 2005; Warburton 2006; Pasquetti

& Rapetti 2006). In particular, recent applications of high order methods for elastic wave propagation problems on triangular and tetrahedral grids can be found in Mercerat et al. (2006); Mercerat & Glinsky (2015). A distinguishing feature of SE methods is that they yield accurate solutions, with negligible dispersion and dissipation errors, using few grid points per wavelength, (De Basabe & Sen 2007). For the acoustic case, the dispersion properties of high-order DG methods have been analyzed in Ainsworth (2004a) and in Ainsworth et al. (2006), while time-stepping stability of continuous and discontinuous finite element methods has been addressed in Mulder et al. (2014). In the elastic case, the dispersive behavior of spectral element methods has been analyzed in Seriani & Oliveira (2008) using a Rayleigh quotient approximation of the eigenvalue problem resulting from the dispersion analysis. Dispersion and dissipation properties of DGSE approximation on quadrilateral grids have been studied using a plane wave analysis in De Basabe et al. (2008) and Antonietti et al. (2012). In Antonietti et al. (2012) a comparison with the Mortar method is also presented. A similar approach has been presented for spectral elements and DGSE approximations on triangular grids by Mazzieri & Rapetti (2012); Liu et al. (2012), and in the references therein, where different sets of interpolating nodes have been compared, and by Antonietti et al. (2016c), where the authors have used the modal boundary adapted functions proposed in Sherwin & Karniadakis (1995). All these works deal with two-dimensional model problems and show that triangular spectral elements feature dispersion and dissipation properties similar to those of the standard tensor product elements.

In this paper we propose a numerical study of dispersion and dissipation properties for the three-dimensional elastodynamics equation discretized with both SE and DGSE approximation on hexahedral and tetrahedral grids. Our analysis is based on the plane wave method and it is applied to the semi discrete as well as the fully discrete formulation, resulting after a leap-frog time integration. For the latter, an analysis of the stability constraint required by the different approaches is also carried out.

The paper is organized as follows. In Section 2 we introduce the elastodynamics problem and its SE and DGSE approximation, as well as the fully discrete scheme resulting after leap-frog integration. In Section 3 we present the dispersion and dissipation analysis, describing the details of the plane wave method for both the continuous and the discontinuous case. Several numerical tests are then presented in Section 4 for the semi discrete problem and in Section 5 for the fully discrete problem, showing dispersion and dissipation errors as a function of different discretization parameters such as the polynomial degree, the spatial and the time step. For the fully discrete case, we also provide a stability analysis of the different methods considered in this work. In Section 6 the presented methods

are then applied to the simulation of a real earthquake scenario. Finally, in Section 7 we draw some conclusions.

2 GOVERNING EQUATIONS AND NUMERICAL DISCRETIZATION

Let Ω be an unbounded isotropic and homogeneous domain. Consider a temporal interval $[0, T]$, with $T > 0$. The dynamic equilibrium for an elastic medium subject to an external force leads to the following equation

$$\rho \partial_{tt} \mathbf{u} - \nabla \cdot \underline{\sigma}(\mathbf{u}) = \mathbf{f} \qquad \text{in } \Omega \times (0, T], \tag{1}$$

coupled with suitable boundary and initial conditions. Here $\rho > 0$ is the medium density, $\mathbf{u} = \mathbf{u}(\mathbf{x}, t)$ is the displacement field, $\underline{\sigma}(\mathbf{u})$ is the stress tensor and $\mathbf{f} = \mathbf{f}(\mathbf{x}, t)$ is a (smooth enough) given external load (e.g., a seismic source). We use the Hooke's law

$$\underline{\sigma}(\mathbf{u}) = \lambda \text{tr}(\underline{\epsilon}(\mathbf{u})) + 2\mu \underline{\epsilon}(\mathbf{u}), \tag{2}$$

as the constitutive equation for the stress tensor $\underline{\sigma}$. In particular $\underline{\epsilon}(\mathbf{u}) = \frac{1}{2}(\nabla \mathbf{u} + \nabla^T \mathbf{u})$ is the strain tensor, λ and μ are the Lamé elastic coefficients and tr$(\cdot)$ is the trace operator. The elastic speed of the compressional waves (c_P), and the elastic speed of the shear waves (c_S) are obtained through the relations

$$c_P = \sqrt{(\lambda + 2\mu)/\rho}, \qquad c_S = \sqrt{\mu/\rho}. \tag{3}$$

2.1 Continuous and discontinuous spectral elements formulations

In the following, we introduce a family of semi discrete approximations to problem (1). We focus on the DG discretization, since the continuous one can be seen as a special case. The semi discrete symmetric interior penalty approximation (see Wheeler (1978); Arnold (1982)) of problem (1) reads: for any $t \in (0, T]$, find $\mathbf{u} = \mathbf{u}(t) \in \mathbf{V}_{DG} = \{\mathbf{u} \in \mathbf{L}^2(\Omega) \ : \mathbf{u} \in \mathbb{P}^N(E) \ \forall \ E \in \mathcal{T}_h\}$ such that

$$\sum_{E \in \mathcal{T}_h} \int_E \rho \mathbf{u}_{tt}(t) \cdot \mathbf{v} \, d\mathbf{x} + \mathcal{A}_h(\mathbf{u}(t), \mathbf{v}) + \mathcal{B}_h(\mathbf{u}(t), \mathbf{v}) = \sum_{E \in \mathcal{T}_h} \int_E \mathbf{f}(t) \cdot \mathbf{v} \, d\mathbf{x} \quad \forall \mathbf{v} \in \mathbf{V}_{DG}, \tag{4}$$

where $\mathcal{T}_h$ is the set of elements E (hexahedra or tetrahedra) that discretize Ω, $\mathbb{P}^N(E)$ is a suitable polynomial space that will be defined later on and

$$\mathcal{A}_h(\mathbf{u},\mathbf{v}) = \sum_{E\in\mathcal{T}_h}\int_E \underline{\sigma}(\mathbf{u}) : \underline{\epsilon}(\mathbf{v})\, d\mathbf{x} \qquad \forall\, \mathbf{u},\mathbf{v}\in\mathbf{V}_{DG}, \tag{5}$$

$$\mathcal{B}_h(\mathbf{u},\mathbf{v}) = \sum_{F\in\mathcal{F}_h}\left(-\int_F \{\underline{\sigma}(\mathbf{u})\} : [\![\mathbf{v}]\!]\, d\mathbf{s} - \int_F [\![\mathbf{u}]\!] : \{\underline{\sigma}(\mathbf{v})\}\, d\mathbf{s} + \int_F \eta_F [\![\mathbf{u}]\!] : [\![\mathbf{v}]\!]\, d\mathbf{s}\right) \quad \forall\, \mathbf{u},\mathbf{v}\in\mathbf{V}_{DG}, \tag{6}$$

where $\mathcal{F}_h$ is the set of faces F of the triangulation $\mathcal{T}_h$. Here, we use the standard notation for the definition of jump $[\![\cdot]\!]$ and average $\{\cdot\}$ operators (see Arnold et al. 2002). On each face $F\in\mathcal{F}_h$ the penalty parameter η_F is defined as

$$\eta_F = \alpha\{\lambda+2\mu\}_A N^2/h_F, \tag{7}$$

where $\{q\}_A = 2q^+q^-/(q^+ + q^-)$ is the harmonic average of the quantity q across F, N is the polynomial degree, h_F is the diameter of the face F and α is a (large enough) positive constant to be properly chosen (see, e.g., Arnold 1982; Arnold et al. 2002; Epshteyn & Rivière 2007).

In the case of a SE approximation the interface term $\mathcal{B}_h(\mathbf{u},\mathbf{v})$ is identically equal to zero and the semi discrete formulation of problem (1) can be written as: for any $t\in(0,T]$, find $\mathbf{u}=\mathbf{u}(t)\in\mathbf{V}_{CG} = \{\mathbf{u}\in\mathbf{C}^0(\Omega)\ : \mathbf{u}\in\mathbb{P}^N(E)\ \forall\ E\in\mathcal{T}_h\}$ such that

$$\sum_{E\in\mathcal{T}_h}\int_E \rho\mathbf{u}_{tt}(t)\cdot\mathbf{v}\, d\mathbf{x} + \mathcal{A}_h(\mathbf{u}(t),\mathbf{v}) = \sum_{E\in\mathcal{T}_h}\int_E \mathbf{f}(t)\cdot\mathbf{v}\, d\mathbf{x} \qquad \forall\mathbf{v}\in\mathbf{V}_{CG}. \tag{8}$$

Error bounds and stability estimates for problem (4) and (8) coupled with suitable boundary conditions can be found for instance in Rivière & Wheeler (2003); Rivière et al. (2007); Antonietti et al. (2012, 2016a,b).

2.2 Algebraic formulation

Let N_{dof} be the number of degrees of freedom per each component of the displacement field $\mathbf{u}$ and let $\{\mathbf{\Psi}_i^\ell\}_{i=1,\dots,N_{dof}}^{\ell=1,2,3}$ be a basis for the finite element space $\mathbf{V}_{DG}$ (or $\mathbf{V}_{CG}$), where $\mathbf{\Psi}_i^1 = (\psi_i,0,0)^T$, $\mathbf{\Psi}_i^2 = (0,\psi_i,0)^T$ and $\mathbf{\Psi}_i^3 = (0,0,\psi_i)^T$, for $i=1,...,N_{dof}$. We express a function $\mathbf{u}\in\mathbf{V}_{DG}$ (or $\mathbf{V}_{CG}$) as linear combination of the basis functions, namely

$$\mathbf{u}(\mathbf{x},t) = \sum_{j=1}^{N_{Dof}}\left(\begin{bmatrix}\psi_j(\mathbf{x})\\0\\0\end{bmatrix}U_j^1(t) + \begin{bmatrix}0\\\psi_j(\mathbf{x})\\0\end{bmatrix}U_j^2(t) + \begin{bmatrix}0\\0\\\psi_j(\mathbf{x})\end{bmatrix}U_j^3(t)\right).$$

Using the above expansion and writing (4) for any test function $\mathbf{\Psi}_i^k$, $k = 1, 2, 3$, $i = 1, ..., N_{dof}$, we obtain the following system of second order ordinary differential equations

$$\underline{M}\ddot{\mathbf{U}} + \underline{K}\mathbf{U} = \mathbf{F}, \tag{9}$$

or, in a blockwise form,

$$\begin{bmatrix} \underline{M}^1 & 0 & 0 \\ 0 & \underline{M}^2 & 0 \\ 0 & 0 & \underline{M}^3 \end{bmatrix} \begin{bmatrix} \ddot{\mathbf{U}}^1 \\ \ddot{\mathbf{U}}^2 \\ \ddot{\mathbf{U}}^3 \end{bmatrix} + \begin{bmatrix} \underline{K}^{1,1} & \underline{K}^{1,2} & \underline{K}^{1,3} \\ \underline{K}^{2,1} & \underline{K}^{2,2} & \underline{K}^{2,3} \\ \underline{K}^{3,1} & \underline{K}^{3,2} & \underline{K}^{3,3} \end{bmatrix} \begin{bmatrix} \mathbf{U}^1 \\ \mathbf{U}^2 \\ \mathbf{U}^3 \end{bmatrix} = \begin{bmatrix} \mathbf{F}^1 \\ \mathbf{F}^2 \\ \mathbf{F}^3 \end{bmatrix}.$$

Each block $\underline{M}^\ell$ of the mass matrix $\underline{M}$ has the following form

$$M_{i,j}^\ell = (\rho \mathbf{\Psi}_j^\ell, \mathbf{\Psi}_i^\ell)_{\mathcal{T}_h} \qquad \ell = 1, 2, 3 \quad i, j = 1, ..., N_{dof}.$$

The entries of the stiffness matrix are given by

$$K_{i,j}^{\ell,m} = \mathcal{A}_h(\mathbf{\Psi}_j^m, \mathbf{\Psi}_i^\ell) + \mathcal{B}_h(\mathbf{\Psi}_j^m, \mathbf{\Psi}_i^\ell) \qquad \ell, m = 1, 2, 3, \quad i, j = 1, ..., N_{dof}.$$

We recall that $\mathcal{B}_h(\cdot, \cdot) \equiv 0$ for SE approximations. Finally, the right-hand side $\mathbf{F}$ has the following expression

$$F_i^\ell = (\mathbf{f}, \mathbf{\Psi}_i^\ell)_{\mathcal{T}_h}, \qquad \ell = 1, 2, 3, \quad i = 1, ..., N_{dof}.$$

Notice that the choice of the basis functions $\{\mathbf{\Psi}_i^\ell\}$ for the finite element space $\mathbf{V}_{DG}$ (or $\mathbf{V}_{CG}$) reflects on the structure of system (9). In the following (for both SE and DGSE approximations) we consider:

- tensor product nodal Lagrangian functions associated with the Gauss-Legendre-Lobatto (GLL) interpolating points for hexahedral elements (see Canuto et al. 2006)
- modal boundary adapted basis functions for tetrahedral elements (see Karniadakis & Sherwin 2005; Sherwin & Karniadakis 1995).

For the latter we report the complete expression of the basis functions in Appendix A.

2.3 Time integration scheme

In this section we briefly present the time marching scheme employed to integrate (9). We subdivide the time interval $(0, T]$ into N_T subintervals of length $\Delta t = T/N_T$ and we denote by $\mathbf{U}^i$ the approximation of $\mathbf{U}$ at time $t_i = i\Delta t$, $i = 0, ..., N_T$. To solve system (9) we employ the second order leap-frog time integration scheme. At the first time step we set

$$\underline{M}\mathbf{U}^1 = (\underline{M} - \frac{\Delta t^2}{2}\underline{K})\mathbf{U}^0 - \Delta t \underline{M}\mathbf{U}^0 + \frac{\Delta t^2}{2}\mathbf{F}^0,$$

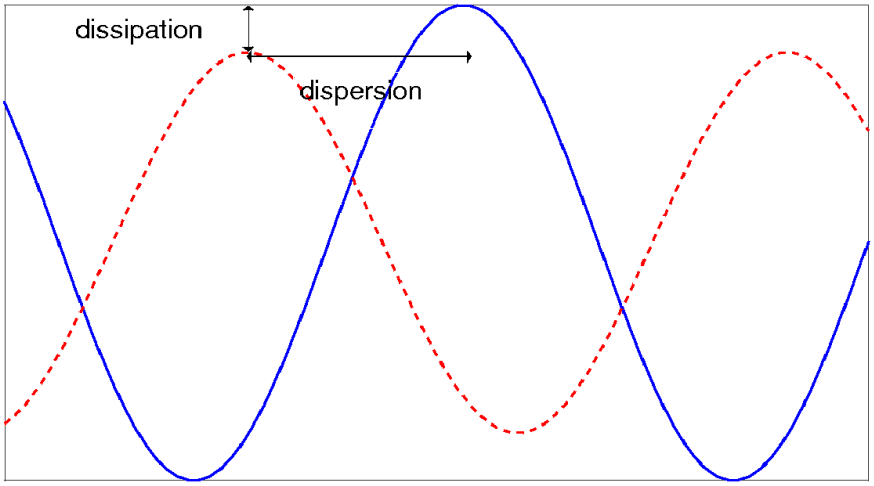

Figure 1. Example of a travelling wave (solid line) and its numerical approximation (dotted line).

and

$$\underline{M}\mathbf{U}^{n+1} = (2\underline{M} - \Delta t^2 \underline{K})\mathbf{U}^n - \underline{M}\mathbf{U}^{n-1} + \Delta t^2 \mathbf{F}^n, \qquad n = 1, ..., N_T - 1, \tag{10}$$

If we consider hexahedral grids, system (10) can be easily inverted, exploiting the diagonal structure of the mass matrix $\underline{M}$, whereas, if we employ tetrahedral grids the matrix $\underline{M}$ is no longer diagonal, so at each time step a suitable direct or iterative method must be used to solve (10). Here, since $\underline{M}$ is symmetric and positive definite (see Quarteroni & Valli 2008), we consider a Cholesky factorization. We recall that the leap-frog method is an explicit second order accurate scheme, therefore to ensure the numerical stability a CFL condition has to be satisfied (see Quarteroni & Valli 2008). In Section 5 we will show a numerical investigation on the stability constraint of the time marching scheme.

3 DISPERSION AND DISSIPATION ANALYSIS: GENERALITIES

The aim of this section is to investigate the dispersion and dissipation errors for the numerical schemes presented before, by considering the propagation of plane waves in a homogeneous medium. We recall that for a plane wave, the discrepancy between the phase of the numerical solution and that of the exact solution is referred to as numerical dispersion, whereas a decrease in the amplitude is referred to as numerical dissipation (cf. Fig. 1). Following Eringen & Şuhubi (1975), in an infinite elastic medium free from body forces, the displacement field is governed by the equation

$$\rho \partial_{tt} \mathbf{u} - \nabla \cdot \underline{\sigma}(\mathbf{u}) = \mathbf{0}. \tag{11}$$

We seek the solution of (11) in the form of a plane wave

$$\mathbf{u}(\mathbf{x}, t) = \mathbf{A}\mathbf{e}^{\mathbf{i}(\mathbf{k}\cdot\mathbf{x} - \omega \mathbf{t})}, \tag{12}$$

where $\mathbf{A} = [A_1, A_2, A_3]^T$ represents the amplitude of the wave, ω the angular frequency and $\mathbf{k} = 2\pi/L(\cos\theta\cos\varphi, \sin\theta\cos\varphi, \sin\varphi)$ the wavenumber vector, L being the wavelength and θ and φ the angles between the direction of propagation and the coordinate axes. Substituting (12) into (11) leads to

$$\left(\frac{\omega^2}{\kappa^2} - c_S^2\right)\mathbf{A} - (c_P^2 - c_S^2)\left(\frac{\mathbf{k}}{\kappa}\cdot\mathbf{A}\right)\frac{\mathbf{k}}{\kappa} = \mathbf{0}, \tag{13}$$

where $\kappa = |\mathbf{k}|$. Hence, the amplitude vector must satisfy the linear system

$$\underline{\mathcal{K}}\mathbf{A} = \mathbf{0},$$

where the elements of the matrix $\underline{\mathcal{K}}$ are of the form

$$\underline{\mathcal{K}}_{ij} = \left(\frac{\omega^2}{\kappa^2} - c_S^2\right)\delta_{ij} - (c_P^2 - c_S^2)\frac{k_i}{\kappa}\frac{k_j}{\kappa}, \quad \text{for } i,j = 1,...,3,$$

being δ the Kronecker symbol. The nontrivial solution is possible if and only if $\det(\underline{\mathcal{K}}) = 0$, or equivalently if

$$\left(\frac{\omega^2}{\kappa^2} - c_S^2\right)^2\left(\frac{\omega^2}{\kappa^2} - c_P^2\right) = 0$$

so that the plane waves can propagate in an inifinte elastic medium with two velocities $\frac{\omega}{\kappa} = c_P$ and $\frac{\omega}{\kappa} = c_S$. If $\frac{\omega}{\kappa} = c_P$, (13) gives $\mathbf{A} = \left(\frac{\mathbf{k}}{\kappa}\cdot\mathbf{A}\right)\frac{\mathbf{k}}{\kappa}$ which implies that the displacement vector associtated with a plane elastic wave propagating with the velocity c_P is in the direction of propagation, i.e., is a longitudinal wave. If $\frac{\omega}{\kappa} = c_S$, (13) is satisfied if $\frac{\mathbf{k}}{\kappa}\cdot\mathbf{A} = 0$, which implies that the displacement vector assiciated with a plane elastic wave propagating with the velocity c_S is in a direction perpendicular to the direction of propagation, i.e., is a transverse or shear wave.

In three dimensions, equation (13) admits three solutions $(\omega_P, \mathbf{A}_P)$, $(\omega_{S1}, \mathbf{A}_{S1})$ and $(\omega_{S2}, \mathbf{A}_{S2})$ defined by the dispersion relations $\omega_P = \kappa c_P$ and $\omega_{S1} = \omega_{S2} = \kappa c_S$. The amplitude vector $\mathbf{A}_P$ is in the direction of $\mathbf{k}$, while $\mathbf{A}_{S1}$ and $\mathbf{A}_{S2}$ are in the plane normal to $\mathbf{k}$ and $\mathbf{A}_{S1} \perp \mathbf{A}_{S2}$.

In order to have a manageable set of parameters to derive dispersion and dissipation relations, in the present analysis we assume that the medium is isotropic, homogeneous, unbounded and source free. Similar assumptions are standard for plane wave analysis (see for instance Cohen 2002; Ainsworth 2004a,b). Although for realistic geophysical applications these assumptions are in general not matched, this analysis provides valuable information to determine the discretization parameters to be used for the numerical simulation. Under these conditions the semi discrete problem (9) becomes

$$\underline{M}\ddot{\mathbf{U}} + \underline{K}\mathbf{U} = \mathbf{0}. \tag{14}$$

We remind that the matrices $\underline{M}$ and $\underline{K}$ have different structures, depending on whether we are employing a SE or a DGSE approximation. Moreover, the components of the vector $\mathbf{U}$ can be either the

nodal values of the approximated solution for SE (resp. DGSE) methods on hexahedral grids or the modal expansion coefficients for SE (resp. DGSE) approximations on tetrahedral grids. Nevertheless, the analysis we present in the next sections is carried out in a general framework and is independent of the basis adopted to span the discrete space.

In the following sections we will use a Cartesian discretization of the domain Ω into non-overlapping cubes having uniform size; we denote the average distance between their verteces by h. The cubes have sides parallel to the coordinate axes in order to generate a periodic tessellation of the domain. In the case of tetrahedral grids each cube is further divided into tetrahedra as shown in the next section.

3.1 Continuous spectral elements

To comply with unboundedness and periodicity, we consider problem (11) posed over the domain $E_{\mathcal{C}} = (-1,1)^3$ and impose periodic boundary conditions on its boundary, consisting of the faces $F_{\mathcal{R}}, F_{\mathcal{L}}, F_{\mathcal{U}}, F_{\mathcal{D}}, F_{\mathcal{F}}, F_{\mathcal{B}}$ (see Figure 2). In the case of a hexahedral mesh the smallest periodic grid is made by a single element $E_{\mathcal{C}}$, whereas with tetrahedral elements it is composed by six tetrahedra (see Figure 2, right) . We consider as test and trial functions in (14) the functions $\mathbf{\Psi}_i^{\ell,E_{\mathcal{C}}}$, $\ell = 1,2,3$, that have support in $E_{\mathcal{C}}$. This leads to a linear system of equations of dimension $3(N+1)^3 \times 3(N+1)^3$, being N the polynomial approximation degree. In order to impose periodic boundary conditions we define J as the set of master indexes (i.e., the degrees of freedom in which we compute the solution) and with $\widehat{J}_F$, $F = \{F_{\mathcal{R}}, F_{\mathcal{U}}, F_{\mathcal{B}}\}$ the set of slave indexes (i.e., where we impose the periodicity condition). Assuming that the solution is a plane wave, we have that

$$U^{\ell}_{\widehat{j}_F} = e^{\beta_F} U^{\ell}_j \quad \ell = 1,2,3 \quad \forall \widehat{j}_F \in \widehat{J}_F, \tag{15}$$

where $\beta_F = \{-ik_x h, -ik_y h, -ik_z h\}$ for $F = \{F_{\mathcal{R}}, F_{\mathcal{U}}, F_{\mathcal{B}}\}$ and $\widehat{j}_F$ is the slave index in $\widehat{J}_F$ corresponding to the master index $j \in J$ on the opposite face (see for example Figure 2).

Imposing the periodicity conditions (15) through a suitable matrix $\Pi \in \mathbb{R}^{3(N+1)^3 \times 3N^3}$ we obtain

$$\underline{\mathcal{M}}\ddot{\mathbf{U}} + \underline{\mathcal{K}}\mathbf{U} = \mathbf{0}, \tag{16}$$

where $\underline{\mathcal{K}}$ and $\underline{\mathcal{M}}$ are given by

$$\underline{\mathcal{K}} = \Pi^T \underline{K} \Pi, \qquad \underline{\mathcal{M}} = \Pi^T \underline{M} \Pi.$$

3.2 Discontinuous spectral elements

For DGSE methods we consider the same periodicity pattern presented in the previous section. The discontinuities are imposed at the interfaces between each periodic element $E_{\mathcal{C}}$ and its neighbors (see Figure 3).

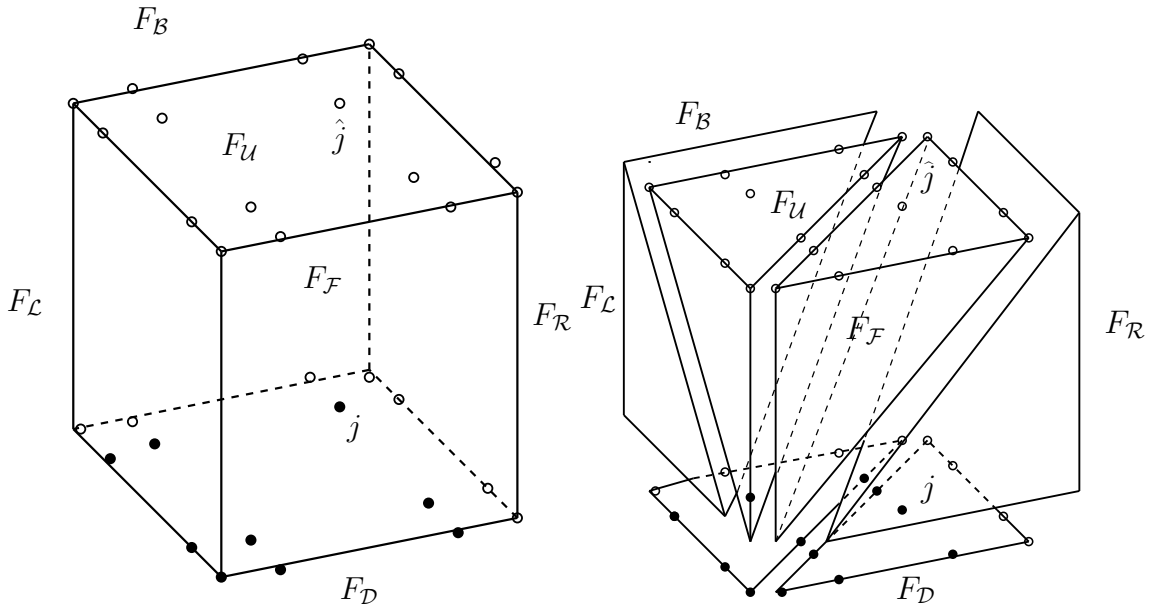

Figure 2. Periodic reference element $E_{\mathcal{C}}$ with faces $\{F_{\mathcal{U}}, F_{\mathcal{D}}, F_{\mathcal{R}}, F_{\mathcal{L}}, F_{\mathcal{F}}, F_{\mathcal{B}}\}$ and smallest pattern of periodic decomposition: hexahedral grid (left) and tetrahedral grid (right). The circles represent the degrees of freedom on top ($F_{\mathcal{U}}$) and bottom ($F_{\mathcal{D}}$) faces for a polynomial degree $N = 3$. Filled circles denote the master degrees of freedom, whereas empty circles denote the slave degrees of freedom where the periodic boundary conditions are imposed.

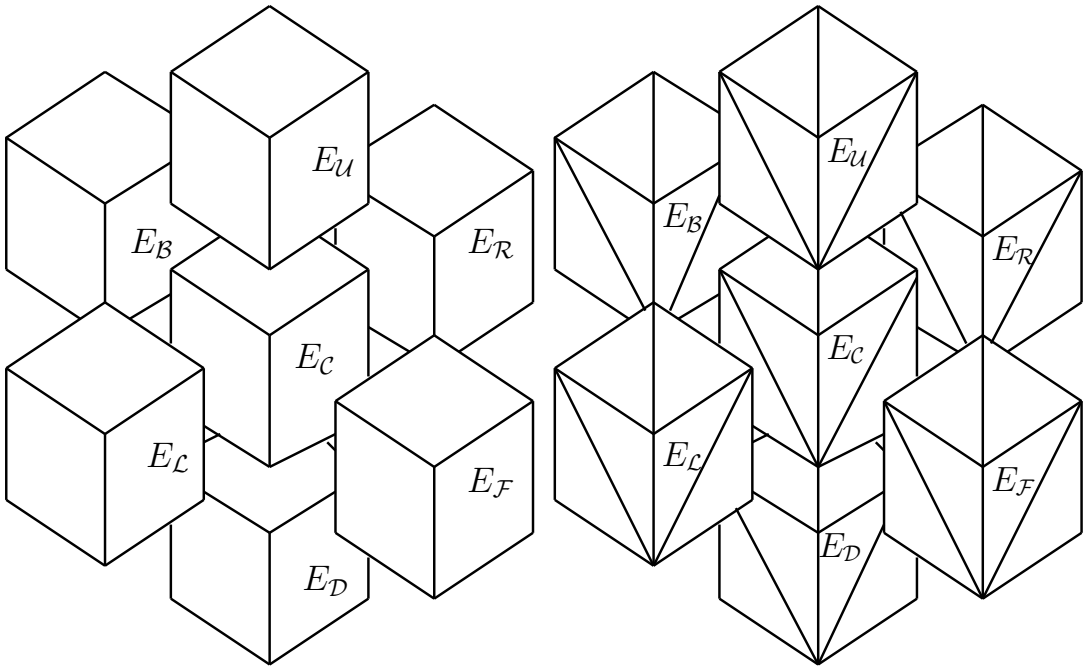

Figure 3. Periodic pattern considered in the discontinuous framework with hexahedral (left) and tetrahedral (right) elements.

Let $\mathbf{\Psi}_i^{\ell,E_f}$, $\ell = 1,2,3$, be the basis functions with support in E_f, with $f = \{\mathcal{C},\mathcal{R},\mathcal{L},\mathcal{U},\mathcal{D},\mathcal{F},\mathcal{B}\}$. Following Mazzieri & Rapetti (2012), we select in (14) as test and trial functions

$$\mathbf{\Psi}_i^{\ell}(\mathbf{x}) = \mathbf{\Psi}_i^{\ell,E_C}(\mathbf{x}) \quad \forall \mathbf{x} \in E_{\mathcal{C}}, \tag{17}$$

$$\mathbf{\Psi}_j^{\ell}(\mathbf{x}) = \begin{cases} \mathbf{\Psi}_j^{\ell,E_{\mathcal{C}}}(\mathbf{x}) & \forall \mathbf{x} \in E_{\mathcal{C}}, \\ \mathbf{\Psi}_j^{\ell,E_f}(\mathbf{x}) & \forall \mathbf{x} \in E_f, f = \{\mathcal{R},\mathcal{L},\mathcal{U},\mathcal{D},\mathcal{F},\mathcal{B}\}, \\ 0 & \text{otherwise.} \end{cases} \tag{18}$$

This choice leads to a rectangular linear system of $21(N+1)^3$ equations in the $3(N+1)^3$ unknowns

$$\mathbf{U}^{\ell} = [\mathbf{U}^{\ell,E_{\mathcal{C}}}, \mathbf{U}^{\ell,E_{\mathcal{R}}}, \mathbf{U}^{\ell,E_{\mathcal{L}}}, \mathbf{U}^{\ell,E_{\mathcal{U}}}, \mathbf{U}^{\ell,E_{\mathcal{D}}}, \mathbf{U}^{\ell,E_{\mathcal{F}}}, \mathbf{U}^{\ell,E_{\mathcal{B}}}], \quad \ell = 1,2,3.$$

Then, the blocks in the mass and stiffness matrices in (14) become

$$\underline{M}^{\ell} = [\underline{M}^{\ell,E_{\mathcal{C}}}, \underline{0}, \underline{0}, \underline{0}, \underline{0}, \underline{0}, \underline{0}], \qquad \ell = 1,2,3, \tag{19}$$

$$\underline{K}^{\ell,m} = [\underline{A}^{\ell,m,E_{\mathcal{C}}} + \underline{B}^{\ell,m,E_{\mathcal{C}}}, \underline{B}^{\ell,m,E_{\mathcal{R}}}, \underline{B}^{\ell,m,E_{\mathcal{L}}}, \underline{B}^{\ell,m,E_{\mathcal{U}}}, \underline{B}^{\ell,m,E_{\mathcal{D}}}, \underline{B}^{\ell,m,E_{\mathcal{F}}}, \underline{B}^{\ell,m,E_{\mathcal{B}}}], \quad \ell, m = 1,2,3, \tag{20}$$

respectively, where

$$\begin{aligned}
\underline{M}_{i,j}^{\ell,E_{\mathcal{C}}} &= \int_{E_{\mathcal{C}}} \rho \mathbf{\Psi}_j^{\ell,E_{\mathcal{C}}} \cdot \mathbf{\Psi}_i^{\ell,E_{\mathcal{C}}}, \\
\underline{A}_{i,j}^{\ell,m,E_C} &= \int_{E_C} \underline{\sigma}(\mathbf{\Psi}_j^{m,E_C}) : \underline{\epsilon}(\mathbf{\Psi}_i^{\ell,E_{\mathcal{C}}}), \\
\underline{B}_{i,j}^{\ell,m,E_{\mathcal{C}}} &= \sum_{f \in \{\mathcal{R},\mathcal{L},\mathcal{T},\mathcal{D},\mathcal{F},\mathcal{B}\}} - \int_{F_f} \{\underline{\sigma}(\mathbf{\Psi}_j^{m,E_{\mathcal{C}}})\} : [\![\mathbf{\Psi}_i^{\ell,E_{\mathcal{C}}}]\!] - \int_{F_f} [\![\mathbf{\Psi}_j^{m,E_{\mathcal{C}}}]\!] : \{\underline{\sigma}(\mathbf{\Psi}_i^{\ell,E_{\mathcal{C}}})\} \\
&\quad + \eta_f \int_{F_f} [\![\mathbf{\Psi}_j^{m,E_{\mathcal{C}}}]\!] : [\![\mathbf{\Psi}_i^{\ell,E_{\mathcal{C}}}]\!], \\
\underline{B}_{i,j}^{\ell,m,E_f} &= - \int_{F_f} \{\underline{\sigma}(\mathbf{\Psi}_j^{m,E_f})\} : [\![\mathbf{\Psi}_i^{\ell,E_{\mathcal{C}}}]\!] - \int_{F_f} [\![\mathbf{\Psi}_j^{m,E_f}]\!] : \{\underline{\sigma}(\mathbf{\Psi}_i^{\ell,E_{\mathcal{C}}})\} \\
&\quad + \eta_f \int_{F_f} [\![\mathbf{\Psi}_j^{m,E_f}]\!] : [\![\mathbf{\Psi}_i^{\ell,E_{\mathcal{C}}}]\!], \qquad f \in \{\mathcal{R},\mathcal{L},\mathcal{T},\mathcal{D},\mathcal{F},\mathcal{B}\}.
\end{aligned}$$

In order to obtain a square linear system we use (12), i.e. the expression of the plane waves. This, together with the imposition of periodic conditions, implies that

$$U_j^{\ell,E_f} = e^{\beta_f} U_j^{\ell,E_{\mathcal{C}}}, \qquad \ell = 1,2,3, \tag{21}$$

where $\beta_f = \{-ik_x h, ik_x h, -ik_z h, ik_z h, ik_y h, -ik_y h\}$ for $f = \{\mathcal{R},\mathcal{L},\mathcal{U},\mathcal{D},\mathcal{F},\mathcal{B}\}$, respectively. Substituting (21) in (19) and (20) leads to the following linear system of $3(N+1)^3$ equations in $3(N+1)^3$ unknowns $\mathbf{U} = \mathbf{U}^{E_{\mathcal{C}}}$:

$$\underline{M}\ddot{\mathbf{U}} + \widetilde{\underline{K}}\mathbf{U} = \mathbf{0}. \tag{22}$$

The components of the matrix $\underline{\tilde{K}}$ are defined as

$$\underline{\widetilde{K}}^{\ell,m} = \underline{A}^{\ell,m,E_{\mathcal{C}}} + \underline{B}^{\ell,m,E_{\mathcal{C}}} + \sum_{f\in\{\mathcal{R},\mathcal{L},\mathcal{U},\mathcal{D},\mathcal{F},\mathcal{B}\}} e^{\beta_f}\underline{B}^{\ell,m,E_f}, \qquad \ell,m = 1,2,3.$$

4 SEMI DISCRETE FORMULATION: DISPERSION AND DISSIPATION ANALYSIS

In this section we analyze the dispersion and dissipation errors introduced by the space discretization. With this aim we assume exact time integration. Taking the second derivative with respect to time in (16) and (22) we find the generalized eigenvalue problems

$$\underline{\mathcal{K}}\mathbf{U} = \omega^2\underline{\mathcal{M}}\mathbf{U}, \tag{23}$$

$$\underline{\widetilde{K}}\mathbf{U} = \omega^2\underline{M}\mathbf{U}, \tag{24}$$

respectively.

4.1 Dispersion analysis

By solving numerically (23) and (24) we obtain the eigenvalues $\xi = \omega_h^2$ that represent the best approximations of the angular frequencies of the travelling waves. The number of eigenvalues obtained through (23) and (24), in general, exceeds the number of physical modes. Then, we identify the numerical eigenvalues ξ_P and ξ_S, corresponding to the physical frequencies, by computing the numerical velocities obtained for each eigenvalue and comparing them to the real values of c_P and c_S, respectively. We remark that the computed eigenvalues approximating ω_{S1} and ω_{S2} are not exactly the same but their difference is negligible (Seriani & Oliveira 2008; Zyserman & Gauzellino 2005). In the following we will select ξ_S as that eigenvalue, between the two physically relevant, that leads to the worst approximation of c_S.

Once selected the eigenvalues ξ_P and ξ_S, we compute the numerical angular frequencies $\omega_{P,h} = \sqrt{\xi_P}$ and $\omega_{S,h} = \sqrt{\xi_S}$ for P- and S-waves, respectively. The numerical wave velocities are therefore given by

$$c_{P,h} = \frac{h\,\omega_{P,h}}{2\pi\delta r}, \qquad c_{S,h} = \frac{h\,\omega_{S,h}}{2\pi\delta},$$

where $\delta = h/(NL)$ is the sampling ratio, i.e. the number of interpolation points per shortest wavelength, L is the wavelength and $r = c_P/c_S$. In the following we consider the relative dispersion errors

$$e_P = \frac{c_{P,h}}{c_P} - 1, \qquad e_S = \frac{c_{S,h}}{c_S} - 1.$$

Note that e_P, $e_S > 0$ implies that the numerical waves propagate faster than the physical ones.

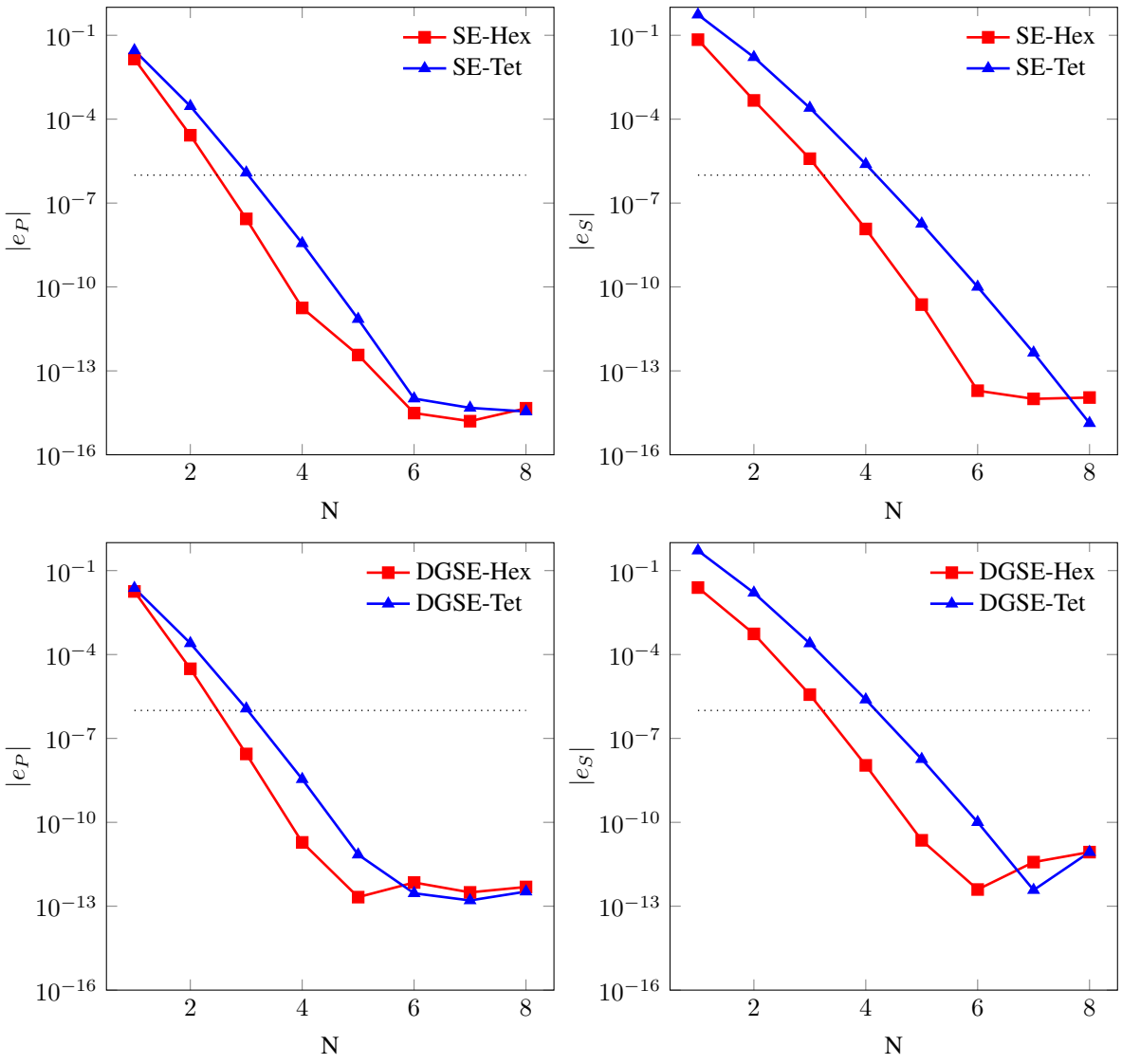

Figure 4. Computed dispersion errors $|e_P|$ and $|e_S|$ versus N with $\delta = 0.2, \theta = \varphi = \pi/4$ and $r = 2$. Continuous spectral elements (SE, top) and discontinuous spectral elements (DGSE, bottom) on both hexahedral (Hex) and tetrahedral (Tet) grids.The superimposed dotted line represents the threshold value 10^{-6}.

NUMERICAL RESULTS

We now investigate how the dispersion errors depend on the polynomial degree N, the sampling ratio δ for the shortest wavelength, the wavenumber vector $\mathbf{k}$ of the plane wave (i.e., the angles θ and φ) and the ratio r. For the DGSE approximation we set the value of the penalty constant $\alpha = 10$, cf. (7). For the first test case, we consider $\delta = 0.2$, i.e., five nodes per shortest wavelength, $\varphi = \theta = \pi/4$ and $r = 2$. Similar results have been obtained for different choices of the angles φ and θ. In Figure 4 we observe, as expected, an exponential decay of the dispersion error with respect to the polynomial degree N, using both SE and DGSE approximations on hexahedral and tetrahedral grids.

For completeness, in Table 1 we report the computed dispersion errors for $r = 2, 5, 10$. Note that the same exponential decay of the dispersion is observed for $r = 5$ and $r = 10$. Moreover, notice that in the considered range of variation for r, negligible dispersion errors (i.e., less than 10^{-6}) can be achieved using a polynomial approximation degree $N \geq 4$ (resp. $N \geq 5$) on hexahedral (resp. tetrahedral) elements for both SE and DGSE approximations.

In Figure 5, we report the computed dispersion errors as a function of δ for different approximation degrees $N = 2, 3, 4$ and $r = 2$. Similar results have been obtained for $r = 5, 10$, cf. Appendix B.

Looking at the slopes of the e_P- and e_S-curves we obtain the following empirical estimate of the orders of convergence, i.e., $e_P = \mathcal{O}(h^{2N})$ and $e_S = \mathcal{O}(h^{2N})$, respectively. These results are in agreement with the quantitative estimates reported in De Basabe et al. (2008) for quadrilateral elements and in (Mazzieri & Rapetti 2012) for triangular elements. For the scalar wave equations, a proof of the order decay for the dispersion errors can be found in Ainsworth (2004a). We notice that a polynomial degree $N = 4$ and 5 points (resp. 10 points) per shortest wavelength are sufficient to achieve a dispersion error less than 10^{-6} for hexahedral (resp. tetrahedral) elements.

Finally, we study the dispersion errors as a function of the angles θ and φ of the plane wave. In Figure 6 we report the results obtained with the DGSE discretization. A similar behavior has been observed for continuous approximations. We set the polynomial degree $N = 3$, the sampling ratio $\delta = 0.2$ and $r = 2$. The same values are used to compute the anisotropy ratios $c_{P,h}/c_P$ and $c_{S,h}/c_S$ that are then projected on the xy, yz and xz planes, see Figure 7. We notice that with hexahedral grids the error behaves symmetrically with respect to the origin of the axes, whereas with tetrahedral grids the error grows along the direction in which the periodic cell E_C is cut into tetrahedra. We also observe that, fixing the threshold value 10^{-6} for the dispersion error, SE on hexahedral elements perform better than those on tetrahedral ones. However, for the latter, a lower dispersion error can be obtained choosing a polynomial approximation degree $N \geq 5$ and five or more points per shortest wavelength, i.e., $\delta \leq 0.2$, see Figures 4 and 5. Moreover, with both kinds of elements, the use of a discontinuous approximation does not introduce significant changes with respect to the continuous one.

4.2 Dissipation analysis

For the dissipation error we study the amplitude of the numerical displacement. Consider as exact solution of (11) the plane wave $e^{i(\mathbf{k}\cdot\mathbf{x}-\omega t)}$. Since $Im(\omega) = 0$, its amplitude is equal to 1 for all times t. On the contrary, the numerical wave will have in general $Im(\omega_h) \neq 0$. Then, we say that the scheme is non dissipative if $Im(\omega_h) = 0$, whereas it is dissipative if $Im(\omega_h) < 0$. In the generalized eigenvalue problems (23) and (24) the mass and the stiffness matrices are symmetric and positive

Table 1. Dispersion errors $|e_P|$ and $|e_S|$ versus N with $\delta = 0.2$, $\theta = \varphi = \pi/4$.

		$r=2$	$r=2$	$r=5$	$r=5$	$r=10$	$r=10$
Scheme	N	$\|e_P\|$	$\|e_S\|$	$\|e_P\|$	$\|e_S\|$	$\|e_P\|$	$\|e_S\|$
	1	1.4148e-02	6.9604e-02	2.6416e-03	2.2721e-01	6.7400e-04	7.9955e-01
	2	2.6593e-05	4.6767e-04	8.0579e-07	6.1213e-04	5.1459e-08	1.0187e-03
	3	2.7218e-08	3.8612e-06	1.3458e-10	2.4279e-06	2.1240e-12	5.4928e-06
SE(Hex)	4	1.7841e-11	1.1863e-08	9.5999e-14	4.1039e-09	1.0697e-13	1.1918e-08
	5	3.6900e-13	2.3394e-11	5.4700e-13	4.1250e-12	1.8079e-12	1.4955e-11
	6	3.1000e-15	1.9546e-14	5.9700e-13	2.8300e-13	1.1762e-12	8.2600e-13
	7	1.5900e-15	9.9992e-15	4.3000e-13	8.6500e-13	3.0453e-13	8.5100e-13
	8	4.6000e-15	1.1132e-14	1.3060e-13	6.8000e-13	5.5668e-13	1.1960e-12
	1	2.8761e-02	5.4539e-01	3.1633e-03	1.4261e+00	7.4217e-04	3.3942e+00
	2	2.9076e-04	1.6397e-02	5.4612e-06	4.0641e-02	3.2238e-07	7.6089e-02
	3	1.2196e-06	2.5159e-04	3.8688e-09	5.8920e-04	5.7394e-11	1.0406e-03
SE(Tet)	4	3.6333e-09	2.4537e-06	1.7950e-12	4.6595e-06	1.9112e-14	6.5672e-06
	5	7.1194e-12	1.8210e-08	8.8904e-15	3.1305e-08	1.0728e-14	4.2130e-08
	6	1.0214e-14	1.0066e-10	6.0417e-15	1.6216e-10	6.1063e-14	2.1043e-10
	7	4.7656e-15	4.4542e-13	2.5758e-14	6.8456e-13	9.3480e-14	8.7057e-13
	8	3.5273e-15	1.3484e-15	2.4713e-15	7.5554e-15	4.9747e-14	7.5915e-14
	1	1.7965e-02	2.4730e-02	3.2328e-03	1.3983e-01	8.3836e-04	5.5843e-01
	2	3.0873e-05	5.4649e-04	9.5317e-07	5.4742e-04	1.4188e-05	1.0709e-03
	3	2.7848e-08	3.6854e-06	1.3747e-10	2.3601e-06	4.1917e-10	6.3220e-06
DGSE(Hex)	4	1.9151e-11	1.0881e-08	1.0873e-12	3.8108e-09	1.4691e-10	1.3644e-07
	5	2.1152e-13	2.2731e-11	5.3141e-13	4.0686e-12	7.2793e-12	1.0787e-09
	6	7.0515e-13	3.9606e-13	2.1557e-12	4.6003e-13	1.0240e-12	7.9154e-11
	7	3.1279e-13	3.7827e-12	3.0416e-12	1.7945e-12	1.2329e-12	6.3425e-12
	8	4.8887e-13	8.6078e-12	6.2175e-13	1.7438e-13	1.6277e-12	7.7889e-12
	1	2.3680e-02	5.1963e-01	2.7931e-03	1.0339e+00	4.6600e-04	2.5904e+00
	2	2.5191e-04	1.6097e-02	4.7095e-06	3.5838e-02	3.0816e-05	7.2009e-02
	3	1.1621e-06	2.4896e-04	3.7104e-09	5.4503e-04	1.4453e-08	1.0154e-03
DGSE(Tet)	4	3.4796e-09	2.4384e-06	1.5481e-12	4.4781e-06	9.9181e-10	6.0659e-06
	5	6.9916e-12	1.8127e-08	5.0860e-13	3.0387e-08	1.5697e-12	1.4970e-08
	6	2.9060e-13	1.0105e-10	1.1298e-12	1.6547e-10	2.4201e-12	1.0200e-09
	7	1.6126e-13	3.7795e-13	1.5655e-12	3.5477e-12	2.7889e-12	6.0330e-11
	8	3.3330e-13	8.6078e-12	5.5490e-13	3.0328e-12	2.3487e-12	2.8487e-11

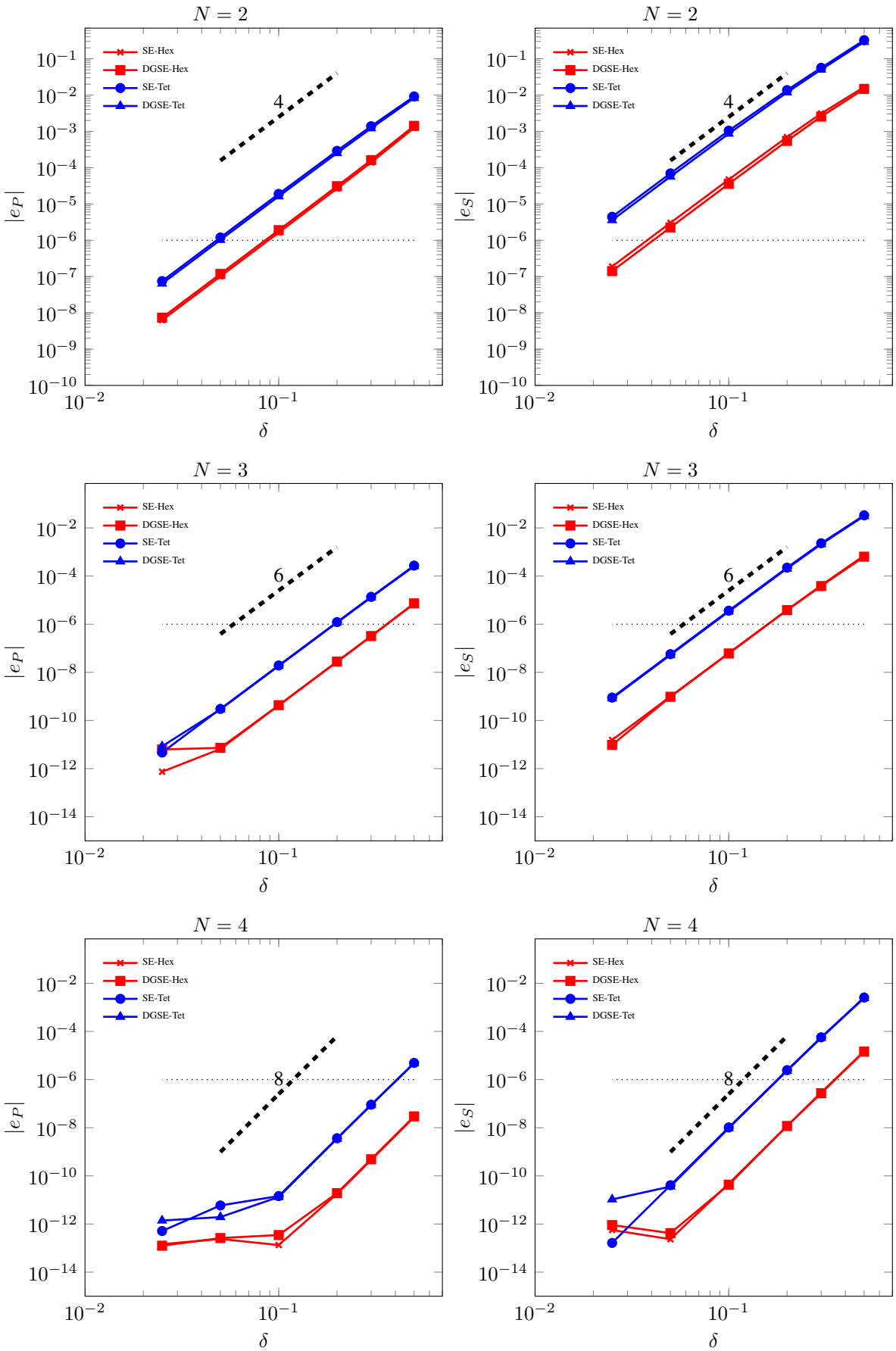

Figure 5. Dispersion errors versus δ for $N = 2, 3, 4$, for continuous spectral elements (SE) and discontinuous spectral elements (DGSE) on both hexahedral (Hex) and tetrahedral (Tet) grids. The superimposed dotted line represents the threshold value 10^{-6}.

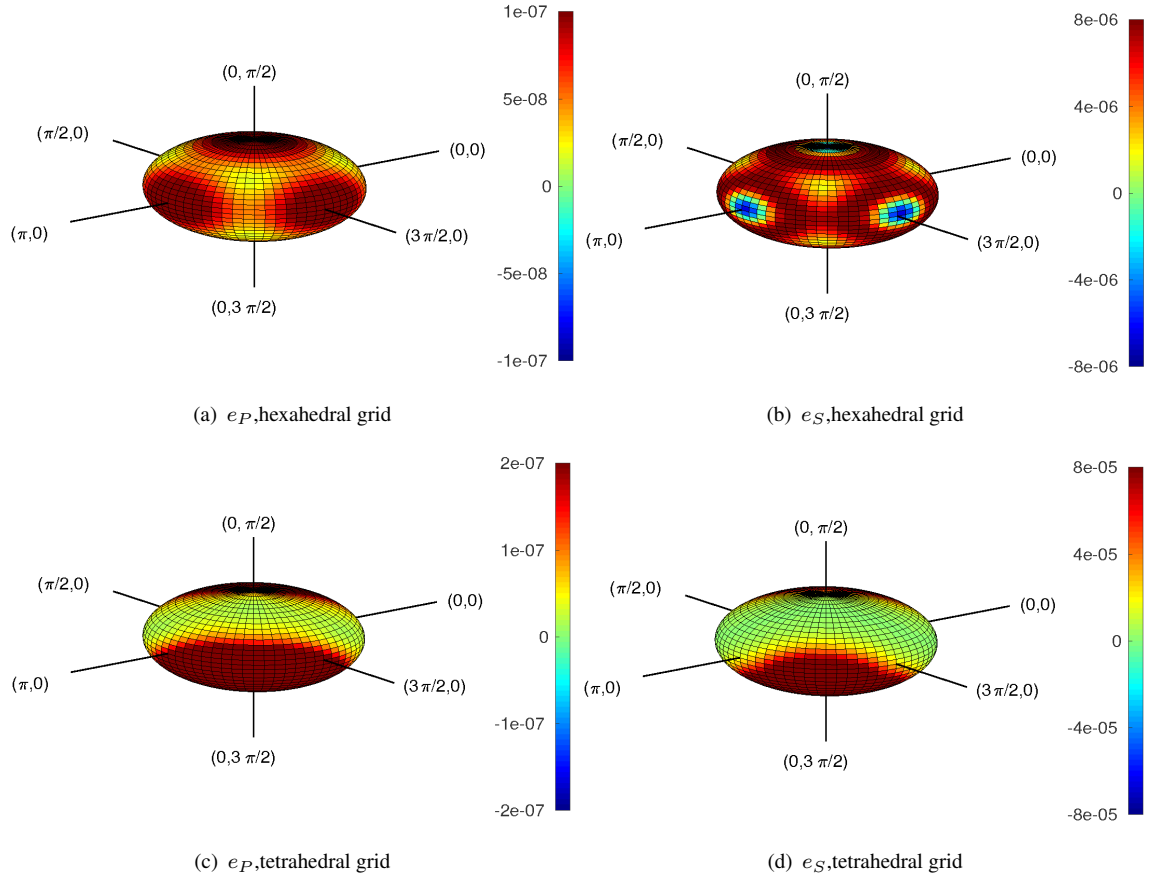

(a) e_P,hexahedral grid (b) e_S,hexahedral grid

(c) e_P,tetrahedral grid (d) e_S,tetrahedral grid

Figure 6. Dispersion errors e_P (left) and e_S (right) as a function of the incidence angles (θ, φ) for DGSE approximation on hexahedral (top) and tetrahedral (bottom) grids.

definite. Therefore, the computed eigenvalues are all real, leading to schemes that do not suffer from dissipation error.

5 FULLY DISCRETE FORMULATION: DISPERSION AND DISSIPATION ANALYSIS

In this section we investigate dispersion and dissipation behaviors of the solution of the fully discrete problem based on employing the leap-frog time integration scheme, cf. Section 2.3. The latter is a typical choice for time integration in the framework of computational seismology, see for instance Cohen (2002); Faccioli et al. (1997); Komatitsch & Tromp (1999). Following Alford et al. (1974), we substitute (12) into (16) and obtain

$$\underline{\mathcal{M}}(e^{-i\omega t_{j+1}} - 2e^{-i\omega t_j} + e^{-i\omega t_{j-1}})\frac{\mathbf{U}_0}{\Delta t^2} + \underline{\mathcal{K}}e^{-i\omega t_j}\mathbf{U}_0 = \mathbf{0}, \quad j = 1, ..., N_T - 1. \tag{25}$$

The above system can be rewritten as

$$\underline{\mathcal{M}}(2 - e^{-i\omega\Delta t} - e^{i\omega\Delta t})\frac{\mathbf{U}_0}{\Delta t^2} = \underline{\mathcal{K}}\mathbf{U}_0.$$

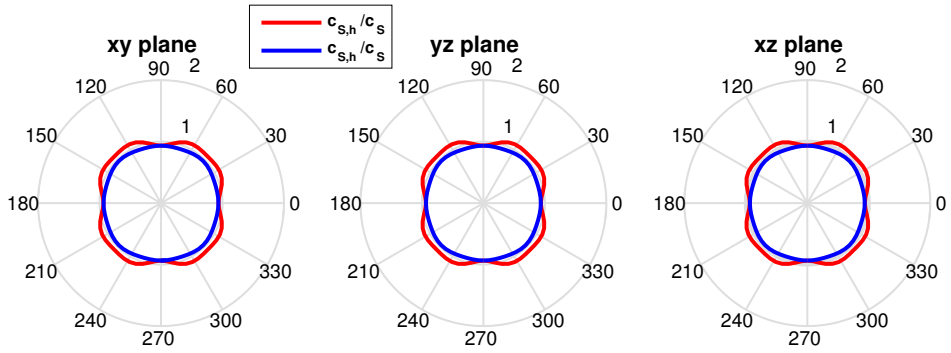

(a) hexahedral grids

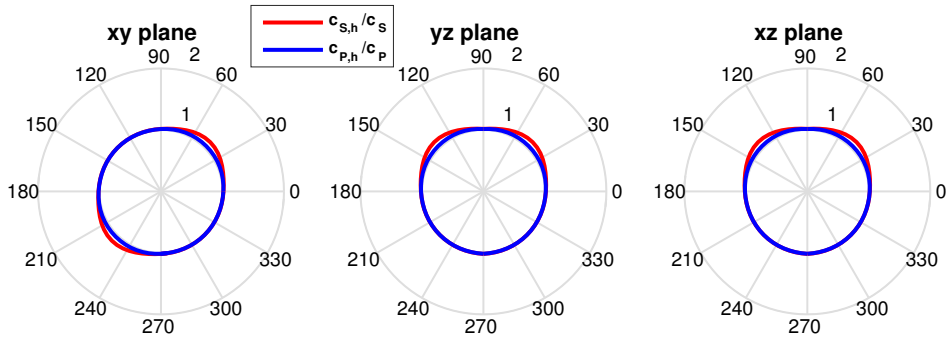

(b) tetrahedral grids

Figure 7. Projections on the xy, yz and xz planes of the anisotropy ratios, $c_{P,h}/c_P$ and $c_{S,h}/c_S$, as a function of the incidence angles (θ, φ) for the DGSE approximation on hexahedral (top) and tetrahedral (bottom) grids. Values are magnified by a factor 10^4.

Now, using the following relation

$$2 - e^{-i\omega\Delta t} - e^{i\omega\Delta t} = 2(\cos(\omega\Delta t) - 1) = 4\sin^2\left(\omega\frac{\Delta t}{2}\right),$$

we obtain a generalized eigenvalue problem of the form

$$\underline{\mathcal{K}}\mathbf{U}_0 = \Lambda\underline{\mathcal{M}}\mathbf{U}_0, \tag{26}$$

where the eigenvalues Λ are related to the numerical angular frequency ω_h through the relation

$$\Lambda = \frac{4}{\Delta t^2}\sin^2(\omega_h\frac{\Delta t}{2}).$$

The same result can be obtained by applying the leap-frog method (10) to (22). Then, the dispersion and the dissipation errors can be computed as described in Section 4.

Before analyzing the dispersion and dissipation errors introduced by the fully discrete formulation, we study the stability properties of the leap-frog time integration scheme. We recall that the latter is a second order accurate and explicit time integrator. Therefore the time step Δt must be chosen in order

to satisfy the Courant, Friedrichs and Lewy (CFL) condition

$$\Delta t \leq C_{CFL}\frac{h}{c_P}, \tag{27}$$

where h is the spatial step, c_P is the P-wave velocity and $0 < C_{CFL} \leq 1$. Here, we want to investigate the dependency of the constant C_{CFL} on the parameters involved in the model (i.e., λ and μ) and on the polynomial degree N.

To this aim, we consider the generalized eigenvalue problem (26). Using a scaling argument, we rewrite the matrices $\underline{\mathcal{K}}$ and $\underline{\mathcal{M}}$ as

$$\widehat{\underline{\mathcal{K}}}\mathbf{U}_0 = \Lambda'\widehat{\underline{\mathcal{M}}}\mathbf{U}_0, \tag{28}$$

where $\Lambda' = (h/\Delta t)^2 \sin^2(\omega_h \Delta t/2)$. We now define the stability parameter q, as

$$q = c_P\frac{\Delta t}{h}.$$

Clearly, the following inequality holds

$$q^2\Lambda' = c_P^2 \sin^2(\frac{\omega_h \Delta t}{2}) \leq c_P^2,$$

that is equivalent to

$$q \leq \frac{c_P}{\sqrt{\Lambda'}} = C_{CFL}(\Lambda'). \tag{29}$$

As stated in De Basabe & Sen (2010), the eigenvalue Λ' depends on the wavenumber vector $\mathbf{k}$ and therefore on the values of the angles θ and φ. Thus, condition (29) can be reformulated as

$$q \leq c^*(\lambda,\mu)\frac{1}{\sqrt{\Lambda'_{max}}} = q_{CFL}, \tag{30}$$

where Λ'_{max} is the maximum eigenvalue of (28), taken with respect to the values of θ and φ. The constant c^* depends on the Lamé parameters λ and μ. Note that, for the DGSE method, c^* is proportional to $\alpha^{-1/2}$ (see Antonietti & Houston 2011), cf. also (7).

NUMERICAL RESULTS

We now present some numerical tests to give a quantitative estimate of the parameter q_{CFL}. We consider $c_P = 1, r = 2, \theta, \varphi \in (0, 2\pi)$ and $\delta = 0.2$. Similar results have been obtained for $r = 5$ and $r = 10$.

In Figure 8 we observe that, for all the methods, the decay rate of q_{CFL} is approximately proportional to N^{-2}. This result is in agreement with the one obtained in De Basabe & Sen (2010); Antonietti et al. (2012, 2016c). In addition, we notice that, for a given polynomial degree, tetrahedral elements are subjected to a more restrictive stability condition, i.e., lower values of q_{CFL} are obtained. In particular, in the case of SE (resp. DGSE) approximation on a tetrahedral grid, the stability parameter

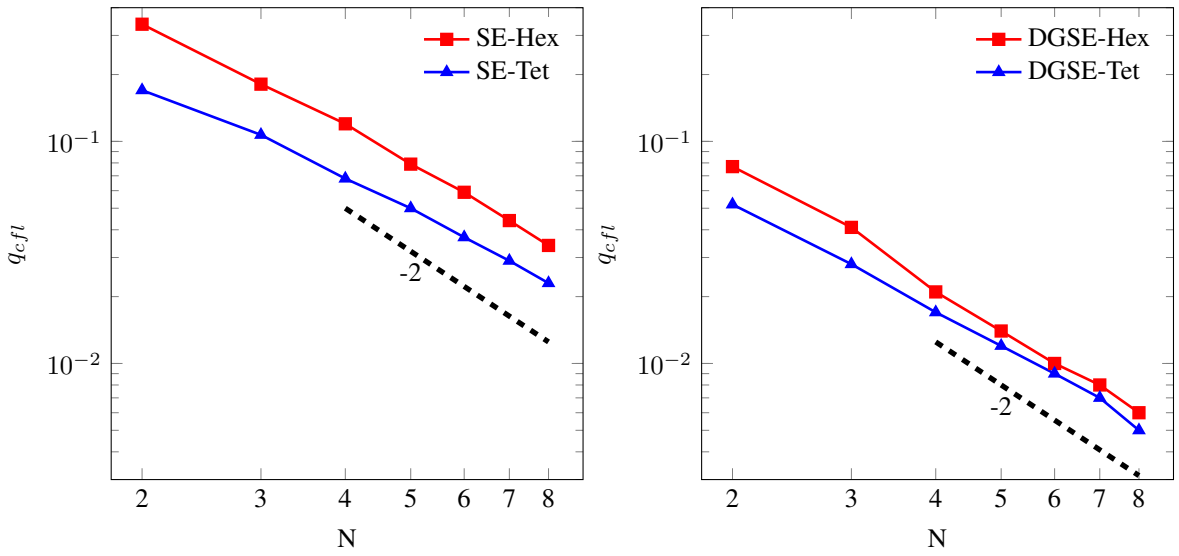

Figure 8. Stability parameter q_{CFL} versus the polynomial degree N for SE (left) and DGSE (right) approximation on both hexahedral and tetrahedral grids.

q_{CFL} is around the 60% (resp. 80%) of the corresponding value computed using a hexahedral mesh. Finally, on the same grid, the CFL condition for the DGSE approximation is always more restrictive than for the SE one. In particular, the stability parameter for the DGSE method is about the 20% of the corresponding SE one on hexahedral grids, and around the 30% of the continuous one on tetrahedral grids.

Now, we present the dispersion and dissipation analysis for the fully discrete approximation, by varying the parameters N, δ and the stability parameter q. In the following, for brevity, we will present only the results related to the DGSE discretization. Similar results have been obtained with the SE approach.

We first address the behavior of the dispersion error with respect to the sampling ratio δ, fixing $N = 4$ and $\theta, \varphi = \pi/4$. We consider the relative stability parameter $q_{rel} = q/q_{CFL}$ in the range $(0.1, 1)$. In practice, for any specific values of N and δ we first compute q_{CFL} according to (30), cf. also Figure 8, then we choose $q \in (0, q_{CFL})$ and finally we calculate the dispersion errors e_P and e_S in terms of q.

As Δt goes to 0, so does q_{rel}, and the fully discrete curves tend to the semi discrete ones (see Figure 9). In Figure 10 we compare the results obtained with both hexahedral and tetrahedral elements with $q_{rel} = 0.2$. We observe that both methods retain the same level of accuracy. In particular for δ<0.2, i.e., five points per wavelength, both methods feature dispersion errors lower than 10^{-6}.

Next, we analyze the dispersion error by varying the polynomial degree N, fixing $\delta = 0.2$ and $\theta, \varphi = \pi/4$. In Figure 11 we observe that, as q_{rel} goes to zero, we retrieve the exponential convergence

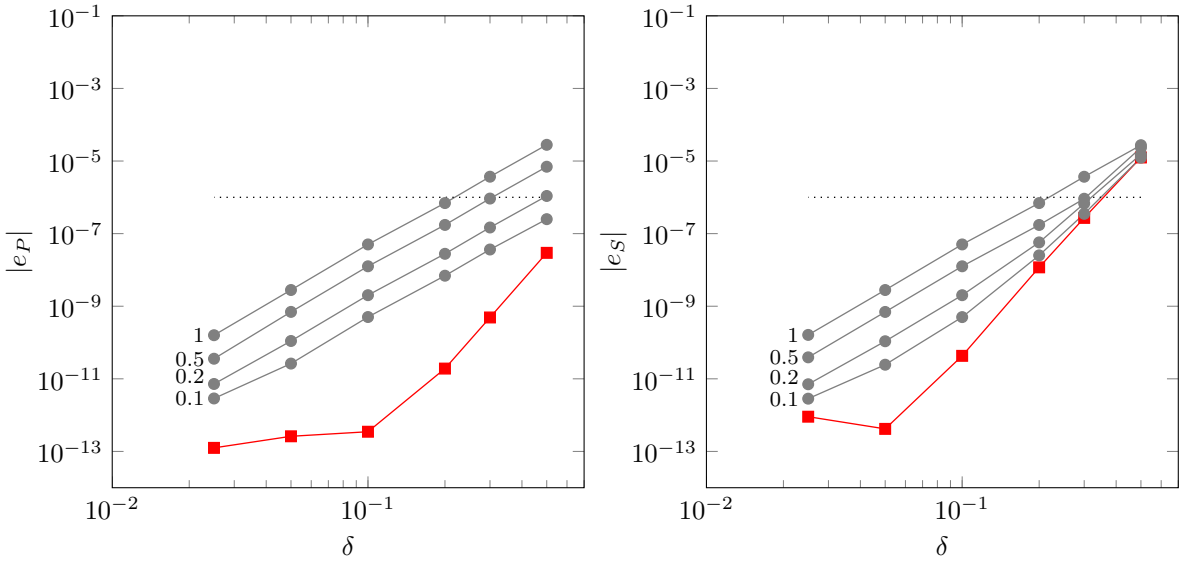

(a) DGSE-Hex

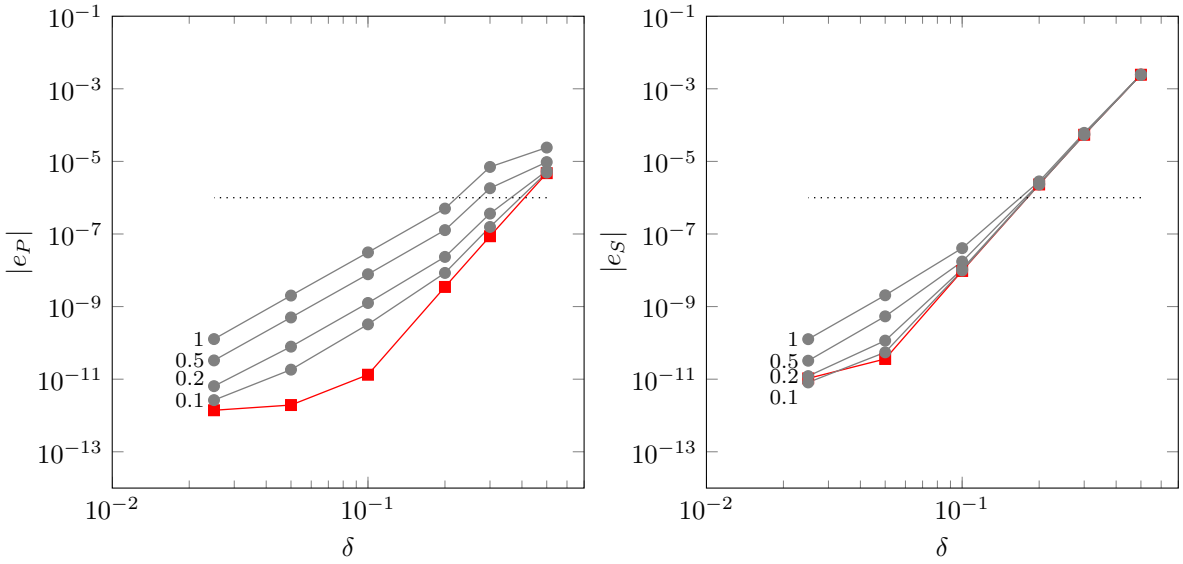

(b) DGSE-Tet

Figure 9. Dispersion errors $|e_P|$ (left) and $|e_S|$ (right) as a function of δ using DGSE on hexahedral (Hex) and tetrahedral (Tet) grids, with a fixed polynomial degree $N = 4$. The square marked red lines refer to the semi discrete approximation, while the others to the fully discrete approximation with $q_{rel} = 0.1, 0.2, 0.5, 1$.

observed in the semi discrete case, cf. Figure 4. Indeed, for sufficiently small values of q, the following asymptotic relation holds

$$\omega_h \approx \sqrt{\Lambda} + \mathcal{O}(\Delta t^2),$$

see also Antonietti et al. (2016c). Thus ω_h decays as in the semi discrete case until the term Δt^2 becomes dominant. In Figure 12 we compare the behavior of the fully discrete scheme obtained on

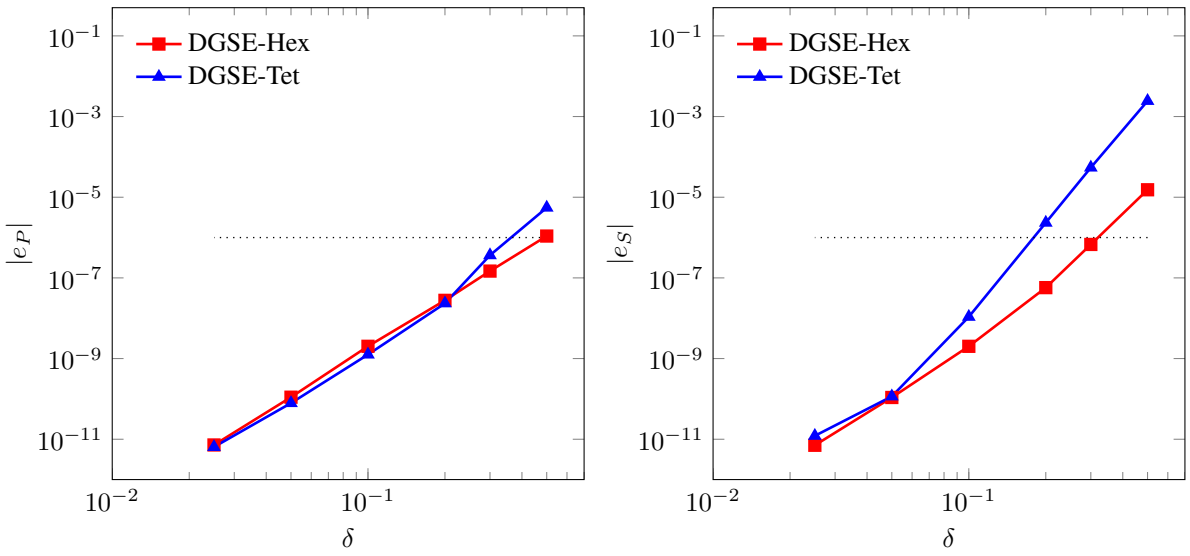

Figure 10. Dispersion errors $|e_P|$ (left) and $|e_S|$ (right) as a function of δ, fixing $N = 4$ and $q_{rel} = 0.2$. DGSE on both hexahedral (Hex) and tetrahedral (Tet) grids.

both hexahedral and tetrahedral grids for $q_{rel} = 0.2$. We notice that the same level of accuracy is obtained on both grids for a polynomial degree $N \geq 5$. Regarding the dissipation error of the fully discrete scheme, the considerations made for the semi discrete case remain valid.

6 A GEOPHYSICAL APPLICATION

In this section we study the seismic response of the Grenoble valley (France), see Figure 13. Due to the sharp contrast in the mechanical properties between the alluvial basin and the surrounding bedrock, and the complex topographical configuration of the region, this test case has been analyzed in several works and using different numerical strategies (see, for example, Chaljub et al. 2007, 2010; Stupazzini et al. 2009). The material properties considered in our simulation are reported in Table 2. In order to exploit the advantages of the numerical methods described in this work, we discretized the domain of about $50\ km \times 47\ km \times 8\ km$ using a hybrid grid made by hexahedral and tetrahedral elements.

Layer	$\rho\ [kg/m^3]$	$c_P\ [km/s]$	$c_S\ [km/s]$
Bedrock	2720	5600	3200
Basin	$2140 + 0.125d$	$1450 + 1.5d$	$300 + 19\sqrt{d}$

Table 2. Mechanical properties for the Grenoble Valley test case. Inside the alluvial basin the mass density and the wave velocities depend on the distance from the surface, denoted here with the letter d.

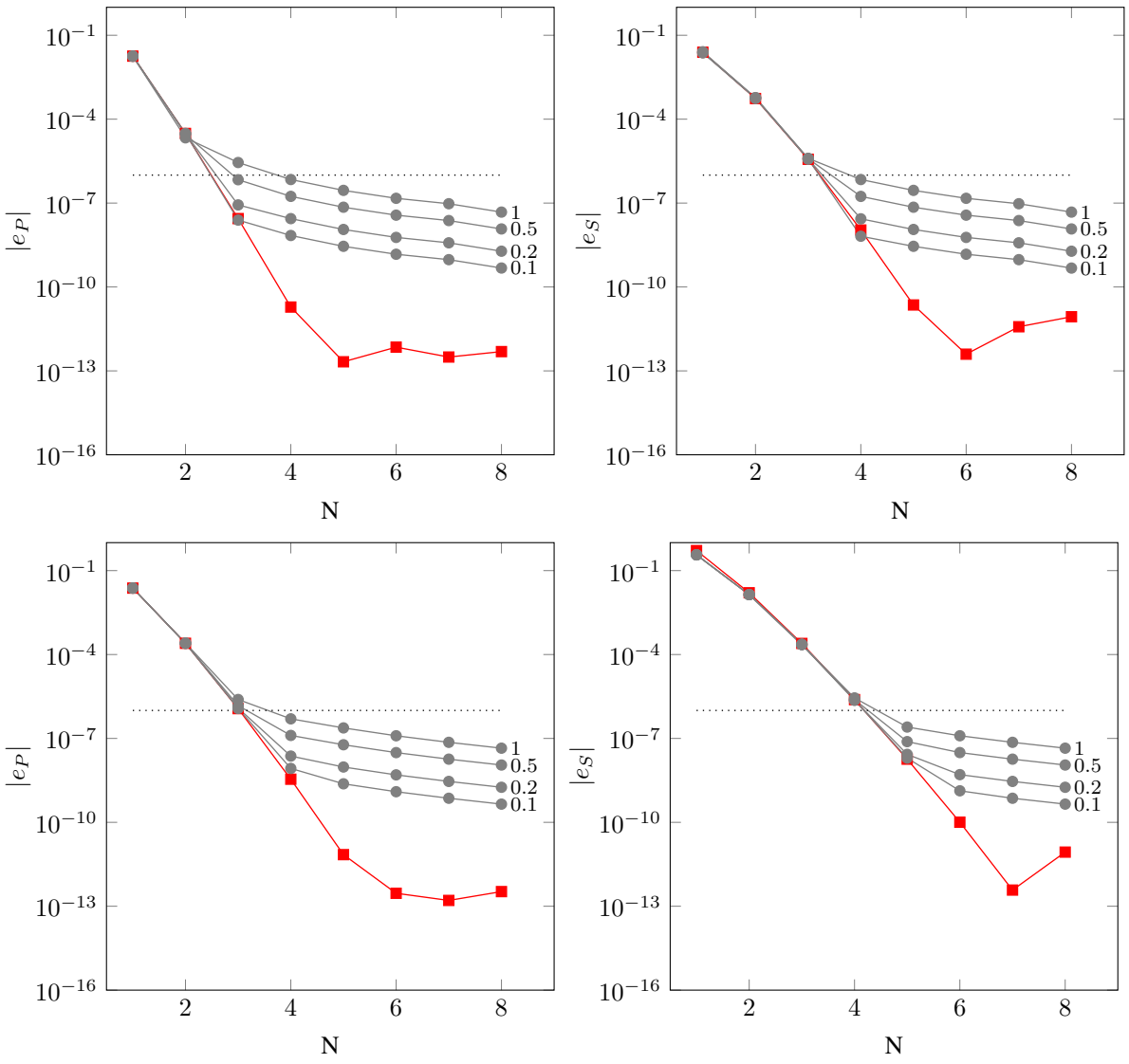

Figure 11. Dispersion errors $|e_P|$ (left) and $|e_S|$ (right) as a function of N, with $\delta = 0.2$, using DGSE on both hexahedral (top) and tetrahedral (bottom) grids. The square marked red lines refer to the semi discrete approximation, while the others to the fully discrete approximation, with $q_{rel} = 0.1, 0.2, 0.5, 1$.

The higher flexibility of tetrahedra is exploited for the triangulation of the alluvial basin, see Figure 14. On the other side, where the geometry of the domain does not feature any significant complexity, hexahedra elements are employed. The resulting computational grid consists of 30590 hexahedral elements of size ranging from 300 m to 900 m and 197905 tetrahedral elements of size approximately 200 m, see Figure 14. As done in Mazzieri et al. (2013), we consider a DGSE discretization in which the DG paradigm is employed only subdomaniwise, i.e., on the surfaces shared by the tetrahedral and the hexahedral meshes. Then, within each macro-area a conforming SE approximation is employed, choosing a polynomial approximation $N = 4$ for hexahedral elements and $N = 3$ for tetrahedral

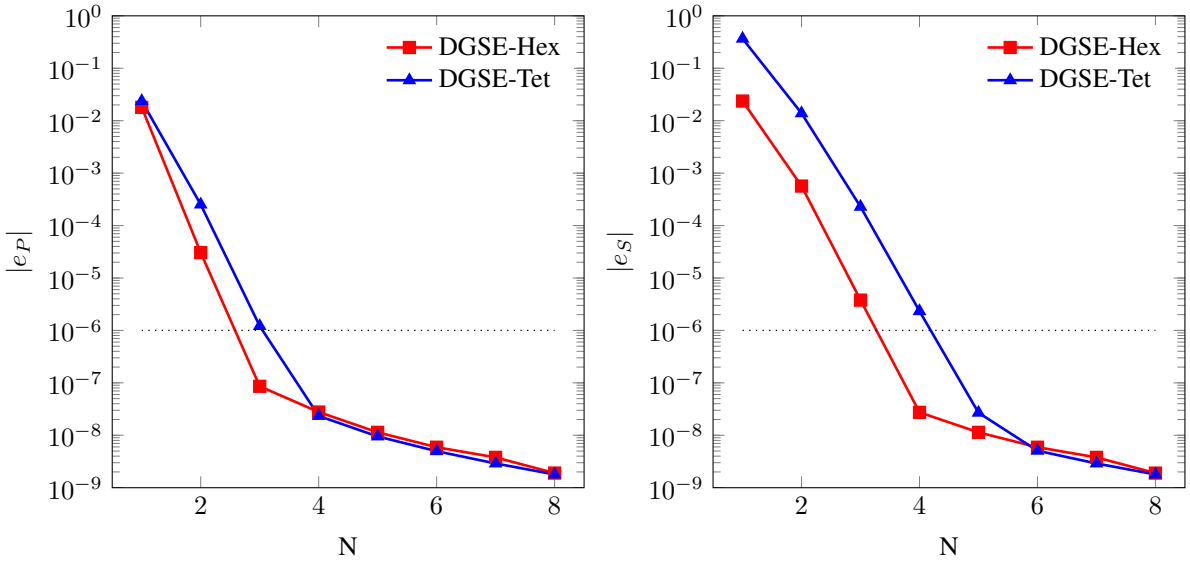

Figure 12. Dispersion errors $|e_P|$ (left) and $|e_S|$ (right) as a function of N with $q_{rel} = 0.2$, using DGSE on both hexahedral (Hex) and tetrahedral (Tet) grids.

ones. This yields to a total number of degrees of freedom equal to 3.1×10^6. We note that the mesh is designed in order to have at least 5 points per shortest wavelength and avoid dispersive effects on the propagation of the wave field, see Section 3. Finally, the model is completed applying a free surface condition on the top surface ($\underline{\sigma}\mathbf{n} = \mathbf{0}$) and absorbing boundary conditions on the remaining boundaries. For the time integration we employ the leap-frog scheme with time step $\Delta t = 2 \times 10^{-4}$ s,

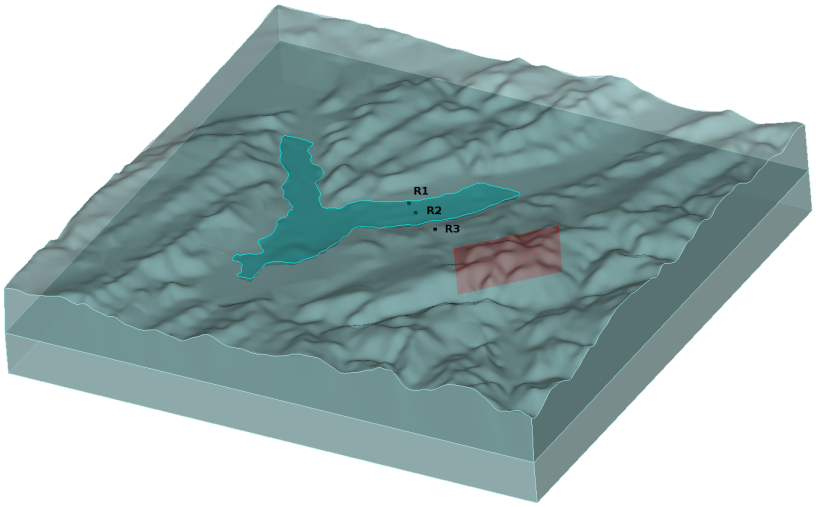

Figure 13. Grenoble Valley test case. The position of the Belledonne border fault is shown in red while that of the soft sediments in cyan. The dots denote the monitors $R1$, $R2$ and $R3$ where we record the numerical solution. $R1$ and $R2$ are located inside the alluvial basin, while $R3$ is in the bedrock.

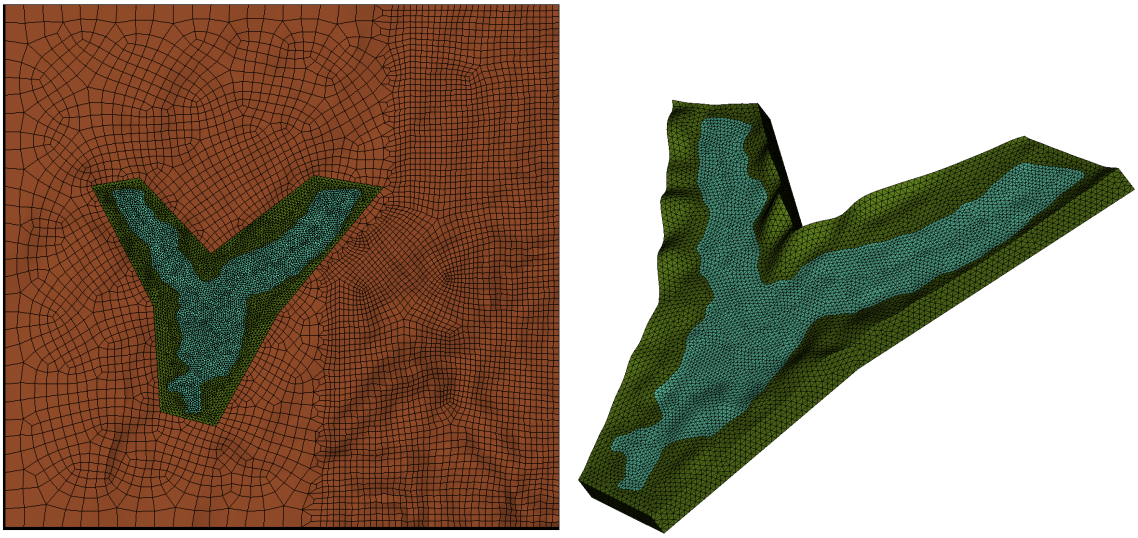

Figure 14. Left: computational domain for the Grenoble Valley test case. The alluvial basin and the surrounding region have been meshed with tetrahedral elements while the rest of the domain has been meshed with hexahedral elements. Right: Detail of the tetrahedral grid used for the basin.

fixing the final time $T = 20\ s$. We study the seismic response to an earthquake of magnitude $M_w \approx 6$ generated by the rupture of the Belledonne fault, see Figure 13. The hypocenter is located at the center of the fault and the rupture velocity is $v_r = 2.8\ km/s$. The time history of the seismic moment M is described by the following function

$$M(t) = \frac{1}{2}\left[1 + \mathrm{erf}\left(2\frac{t-\tau_0}{2\tau_0}\right)\right],$$

where $\mathrm{erf}(\cdot)$ is the error function and $\tau_0 = 0.7\ s$ is the rise time. Further details can be found in Stupazzini et al. (2009).

In Figure 15 we show the components of the displacement field recorded at $R1$, $R2$ and $R3$ (cf. Figure 13) and we compare them with the ones obtained from the simulation using the numerical code SPEED (Mazzieri et al. 2013, http://speed.mox.polimi.it) for a fully conforming hexahedral grid, cf. Stupazzini et al. (2009). The numerical solution obtained with the hybrid grid is recovered by solving at each time step a block-diagonal linear system of the form (10) where the mass matrix can be split as

$$\underline{M} = \begin{pmatrix} \underline{M}_{hex} & \underline{0} \\ \underline{0} & \underline{M}_{tet} \end{pmatrix}.$$

Here $\underline{M}_{hex}$ refers to the unknowns on the hexahedral mesh while $\underline{M}_{tet}$ on the tetrahedral one. Thanks to the choice of the finite element spaces made in Section 2.2, $\underline{M}_{hex}$ is a symmetric and positive definite (spd) diagonal matrix, while $\underline{M}_{tet}$ is still a spd matrix but no longer diagonal and its sparsity pattern depends on the vertex connectivity, see Karniadakis & Sherwin (2005). Then, to solve the

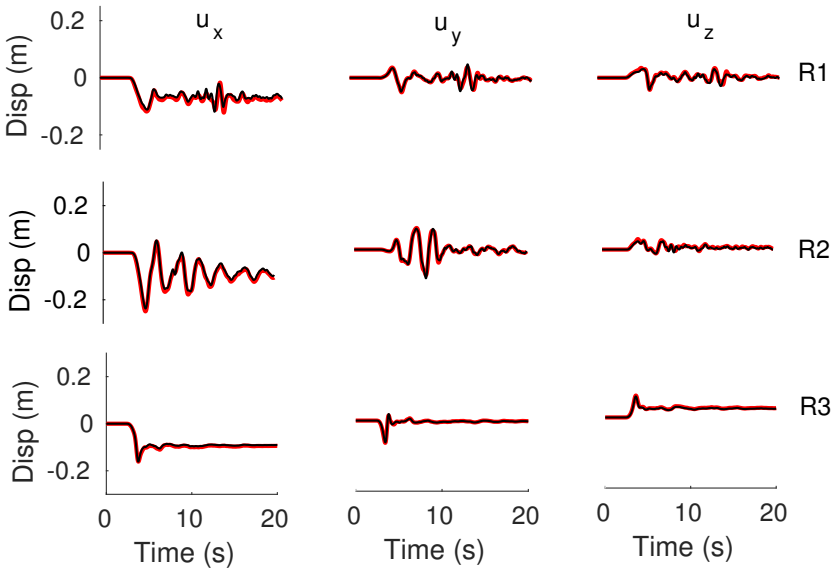

Figure 15. Displacement field recorded at $R1$, $R2$ and $R3$ for the Grenoble Valley test case. The black lines denote the solution computed with the hybrid grid, the red lines the solution obtained with the SPEED code.

linear system with matrix $\underline{M}_{tet}$ we used a Cholesky factorization provided by the numerical library PETSc (`https://www.mcs.anl.gov/petsc/`).

All the simulations have been carried out with 32 cores on the Gigat cluster located at the Politecnico di Milano (`https://hpc.mox.polimi.it/hardware/`) for a total walltime of 90 $hours$ (resp. 11 $hours$) for the hybrid (resp. hexahedral) grid. A very good agreement between the numerical solution obtained with the hybrid grid and the SPEED one is observed (cf. Figure 15). Finally, we note that the highest oscillations for the displacement field are recorded by monitor R2 placed in the middle of the Grenoble alluvial basin.

7 CONCLUSIONS

In this paper we have presented a comprehensive dispersion and dissipation numerical analysis for three dimensional elastic wave propagation problems discretized using both discontinuous and continuous spectral element methods on hexahedral and tetrahedral grids. Our analysis focused on both the semi discrete and the fully discrete formulations, the latter being obtained with the leap-frog time integration scheme. Our results show that all the considered techniques retain very low dispersion and dissipation errors. In particular, we can conclude that:

- for both continuous and discontinuous spectral element methods the computed dispersion error on hexahedral meshes are lower than the corresponding ones computed on tetrahedral meshes;

- both continuous and discontinuous spectral element methods show negligible dispersion errors (i.e., less than 10^{-6}), provided that a polynomial degree $N \geq 4$ and more than 5 (10 resp.) points per wavelength are employed on hexahedral (tetrahedral resp.) grids;

- when coupled with the leap-frog time integration scheme, discontinuous spectral element methods have a more restrictive CFL condition than continuous SE on the same grid. In general, continuous (resp. discontinuous) approximations on tetrahedral grids feature a numerical stability constraint more severe than continuous (resp. discontinuous) discretization on hexahedral grids

- the leap-frog time integration scheme does not introduce any further significant dispersion and dissipation errors to those arising from space discretization. Indeed, the error curves follow the ones obtained in the semi discrete case until the time discretization error becomes dominant.

Finally, we combined the advantages of the different approaches to perform a simulation of geophysical interest. Since geophysical applications are often carachterized by complicated geometries, the flexibility of tetrahedral mesh can drastically simplify the process of the mesh generation. On the other hand, from a computational point of view, continuous and discontinuous approximations on hexahedral meshes seem to be more efficient then the corresponding ones on tetrahedra. This is more evident if an explicit time integration scheme is adopted for the temporal discretization. However, this comparison is beyond the scope of our work and it will be the subject of a future research.

ACKNOWLEDGMENTS

Paola F. Antonietti and Ilario Mazzieri have been partially supported by the SIR Research Grant n. RBSI14VT0S "PolyPDEs Non-conforming polyhedral finite element methods for the approximation of partial differential equations" funded by MIUR - Italian Ministry of Education, Universities and Research. The authors want to express their gratitude to Jonas de Basabe and to the two anonymous Reviewers for the fruitful comments which greatly contributed to the improvement of the manuscript.

APPENDIX A: BASIS FUNCTIONS FOR TETRAHEDRAL ELEMENTS

We consider the reference tetrahedron $\widehat{E}_T$ and the collapsed reference system (η_1, η_2, η_3) as defined in Section 2. Identifying with A, B, C and D the vertices $(-1,-1,-1)$, $(-1,1,-1)$, $(1,-1,-1)$ and $(-1,-1,1)$ (see Figure A1), respectively, the basis functions for the space $\mathbb{P}^{\mathbb{N}}(\widehat{E}_T)$ have the following form

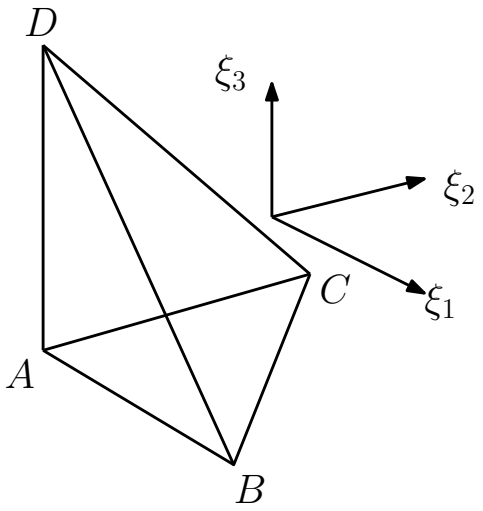

Figure A1. Reference tetrahedron

$$\text{Vertex A}: \left(\frac{1-\eta_1}{2}\right)\left(\frac{1-\eta_2}{2}\right)\left(\frac{1-\eta_3}{2}\right),$$

$$\text{Vertex B}: \left(\frac{1+\eta_1}{2}\right)\left(\frac{1-\eta_2}{2}\right)\left(\frac{1-\eta_3}{2}\right),$$

$$\text{Vertex C}: \left(\frac{1+\eta_2}{2}\right)\left(\frac{1-\eta_3}{2}\right),$$

$$\text{Vertex D}: \left(\frac{1+\eta_3}{2}\right),$$

$$\text{Edge AB}: \left(\frac{1-\eta_1}{2}\right)\left(\frac{1+\eta_1}{2}\right)P_{p-1}^{1,1}(\eta_1)\left(\frac{1-\eta_2}{2}\right)^{p+1}\left(\frac{1-\eta_3}{2}\right)^{p+1}, \qquad 0<p<N,$$

$$\text{Edge AC}: \left(\frac{1-\eta_1}{2}\right)\left(\frac{1-\eta_2}{2}\right)\left(\frac{1+\eta_2}{2}\right)P_{p-1}^{1,1}(\eta_2)\left(\frac{1-\eta_3}{2}\right)^{p+1}, \qquad 0<p<N,$$

$$\text{Edge BC}: \left(\frac{1+\eta_1}{2}\right)\left(\frac{1-\eta_2}{2}\right)\left(\frac{1+\eta_2}{2}\right)P_{p-1}^{1,1}(\eta_2)\left(\frac{1-\eta_3}{2}\right)^{p+1}, \qquad 0<p<N,$$

$$\text{Edge AD}: \left(\frac{1-\eta_1}{2}\right)\left(\frac{1-\eta_2}{2}\right)\left(\frac{1-\eta_3}{2}\right)\left(\frac{1+\eta_3}{2}\right)P_{p-1}^{1,1}(\eta_3), \qquad 0<p<N,$$

$$\text{Edge BD}: \left(\frac{1+\eta_1}{2}\right)\left(\frac{1-\eta_2}{2}\right)\left(\frac{1-\eta_3}{2}\right)\left(\frac{1+\eta_3}{2}\right)P_{p-1}^{1,1}(\eta_3), \qquad 0<p<N,$$

$$\text{Edge CD}: \left(\frac{1+\eta_2}{2}\right)\left(\frac{1-\eta_3}{2}\right)\left(\frac{1+\eta_3}{2}\right)P_{p-1}^{1,1}(\eta_3), \qquad 0<p<N,$$

$$\text{Face ABC}: \left(\frac{1-\eta_1}{2}\right)\left(\frac{1+\eta_1}{2}\right)P_{p-1}^{1,1}(\eta_1)\left(\frac{1-\eta_2}{2}\right)^{p+1}\left(\frac{1+\eta_2}{2}\right) P_{q-1}^{2p+1,1}(\eta_2)\left(\frac{1-\eta_3}{2}\right)^{p+q+1}, \qquad 0<p,q,p+q<N,$$

$$\text{Face ABD}: \left(\frac{1-\eta_1}{2}\right)\left(\frac{1+\eta_1}{2}\right)P_{p-1}^{1,1}(\eta_1)\left(\frac{1-\eta_2}{2}\right)^{p+1}\left(\frac{1-\eta_3}{2}\right)^{p+1} P_{q-1}^{2p+1,1}(\eta_3)\left(\frac{1+\eta_3}{2}\right), \qquad 0<p,q,p+q<N,$$

$$\text{Face ACD}: \left(\frac{1-\eta_1}{2}\right)\left(\frac{1-\eta_2}{2}\right)\left(\frac{1+\eta_2}{2}\right)P_{p-1}^{1,1}(\eta_2)\left(\frac{1-\eta_3}{2}\right)^{p+1} P_{q-1}^{2p+1,1}(\eta_3)\left(\frac{1+\eta_3}{2}\right), \qquad 0<p,q,p+q<N,$$

$$\text{Face BCD}: \left(\frac{1+\eta_1}{2}\right)\left(\frac{1-\eta_2}{2}\right)\left(\frac{1+\eta_2}{2}\right)P_{p-1}^{1,1}(\eta_2)\left(\frac{1-\eta_3}{2}\right)^{p+1} P_{q-1}^{2p+1,1}(\eta_3)\left(\frac{1+\eta_3}{2}\right), \qquad 0<p,q,p+q<N,$$

$$\text{Interior}: \left(\frac{1-\eta_1}{2}\right)\left(\frac{1+\eta_1}{2}\right)P_{p-1}^{1,1}(\eta_1)\left(\frac{1-\eta_2}{2}\right)^{p+1}\left(\frac{1+\eta_2}{2}\right) P_{q-1}^{2p+1,1}(\eta_2)\left(\frac{1-\eta_3}{2}\right)^{p+q+1}\left(\frac{1+\eta_3}{2}\right)P_{r-1}^{2p+2q+1,1}, \qquad 0<p,q,r,p+q+r<N,$$

where $P_p^{\alpha,\beta}$ is the Jacobi polynomial of degree p and parameter α and β (see Karniadakis & Sherwin 2005).

APPENDIX B: DISPERSION ERRORS

In Tables A1–A3 we report the computed dispersion errors for different ratios r and polynomial degrees $N = 2, 3, 4$. It is possible to see that, for a threshold value 10^{-6}, continuous or discontinuous spectral element approximations on tetrahedral meshes achieve the same level of accuracy of the ones on hexahedral meshes by doubling the number of grid points per wavelength.

REFERENCES

Ainsworth, M., 2004a. Discrete dispersion relation for hp-version finite element approximation at high wave number, *SIAM Journal on Numerical Analysis*, **42**(2), 553–575.

Ainsworth, M., 2004b. Dispersive and dissipative behaviour of high order discontinuous Galerkin finite element methods, *Journal of Computational Physics*, **198**(1), 106–130.

Table A1. Dispersion errors $|e_P|$ and $|e_S|$ versus δ, for $\theta = \varphi = \pi/4$ and $N = 2$.

		$r = 5$	$r = 5$	$r = 10$	$r = 10$
Scheme	δ	$\|e_P\|$	$\|e_S\|$	$\|e_P\|$	$\|e_S\|$
	0.5	3.619191e-05	3.472145e-03	2.291422e-06	5.971229e-03
	0.3	4.202135e-06	1.606202e-03	2.679935e-07	2.281569e-03
SE(Hex)	0.2	8.057968e-07	6.121386e-04	5.145953e-08	1.018705e-03
	0.1	4.951748e-08	6.986402e-05	3.164330e-09	1.803446e-04
	0.05	3.082293e-09	5.376082e-06	1.983705e-10	1.951604e-05
	0.025	1.909752e-10	3.561216e-07	8.202999e-12	1.486019e-06
	0.5	1.993511e-04	5.210017e-01	1.201294e-05	5.261674e-01
	0.3	2.717087e-05	1.515186e-01	1.612351e-06	2.475149e-01
SE(Tet)	0.2	5.461212e-06	4.064146e-02	3.223818e-07	7.608952e-02
	0.1	3.450736e-07	3.751011e-03	2.030328e-08	9.634380e-03
	0.05	2.162735e-08	2.758926e-04	1.271330e-09	8.930813e-04
	0.025	1.352288e-09	1.810604e-05	7.892531e-11	6.455328e-05
	0.5	4.205873e-05	2.985762e-03	6.565290e-05	5.903668e-03
	0.3	4.948033e-06	1.469439e-03	3.021277e-05	2.341416e-03
DGSE(Hex)	0.2	9.531727e-07	5.474239e-04	1.418814e-05	1.070958e-03
	0.1	5.873777e-08	5.934822e-05	3.654116e-06	2.149320e-04
	0.05	3.658535e-09	4.446216e-06	9.200300e-07	3.579418e-05
	0.025	2.281916e-10	2.920384e-07	2.304098e-07	6.698034e-06
	0.5	1.755100e-04	5.189609e-01	1.948487e-04	5.256042e-01
	0.3	2.356549e-05	1.378329e-01	6.949580e-05	2.379843e-01
DGSE(Tet)	0.2	4.709577e-06	3.583848e-02	3.081635e-05	7.200907e-02
	0.1	2.964744e-07	3.098995e-03	7.694906e-06	8.745869e-03
	0.05	1.856804e-08	2.196587e-04	1.923209e-06	8.192082e-04
	0.025	1.160309e-09	1.423756e-05	4.807489e-07	7.196206e-05

Ainsworth, M., Monk, P., & Muniz, W., 2006. Dispersive and dissipative properties of discontinuous Galerkin finite element methods for the second-order wave equation, *Journal of Scientific Computing*, **27**(1-3), 5–40.

Alford, R., Kelly, K., & Boore, D. M., 1974. Accuracy of finite-difference modeling of the acoustic wave equation, *Geophysics*, **39**(6), 834–842.

Antonietti, P. F. & Houston, P., 2011. A class of domain decomposition preconditioners for hp-discontinuous Galerkin finite element methods, *Journal of Scientific Computing*, **46**(1), 124–149.

Antonietti, P. F., Mazzieri, I., Quarteroni, A., & Rapetti, F., 2012. Non-conforming high order approximations of the elastodynamics equation, *Computer Methods in Applied Mechanics and Engineering*, **209**, 212–238.

Table A2. Dispersion errors $|e_P|$ and $|e_S|$ versus δ, for $\theta = \varphi = \pi/4$ and $N = 3$.

		$r = 5$	$r = 5$	$r = 10$	$r = 10$
Scheme	δ	$\lvert e_P\rvert$	$\lvert e_S\rvert$	$\lvert e_P\rvert$	$\lvert e_S\rvert$
	0.5	3.511736e-08	1.433108e-04	5.618395e-10	2.068328e-04
	0.3	1.553081e-09	1.813086e-05	2.489510e-11	3.180250e-05
SE(Hex)	0.2	1.345828e-10	2.427962e-06	2.124000e-12	5.492854e-06
	0.1	2.291874e-12	5.245453e-08	1.056829e-12	1.776522e-07
	0.05	1.435699e-12	9.015835e-10	6.616581e-13	3.721776e-09
	0.025	6.844267e-12	1.344032e-11	1.139441e-13	5.030272e-11
	0.5	9.184614e-07	5.974867e-02	1.380467e-08	7.647250e-02
	0.3	4.378294e-08	5.029581e-03	6.511671e-10	7.406337e-03
SE(Tet)	0.2	3.868871e-09	5.892091e-04	5.739431e-11	1.040684e-03
	0.1	6.067014e-11	1.151596e-05	1.038725e-12	2.917990e-05
	0.05	8.992809e-13	1.918991e-07	6.017525e-13	5.863814e-07
	0.025	1.906500e-13	3.049073e-09	2.456265e-12	9.890538e-09
	0.5	3.602552e-08	1.364329e-04	8.626402e-09	2.159940e-04
	0.3	1.590548e-09	1.756871e-05	1.925627e-09	3.427397e-05
DGSE(Hex)	0.2	1.374730e-10	2.360172e-06	4.191714e-10	6.322060e-06
	0.1	3.188954e-12	5.106492e-08	2.406429e-11	2.777673e-07
	0.05	3.823393e-12	8.792009e-10	3.586946e-11	1.203601e-08
	0.025	3.090032e-11	3.613248e-11	9.559023e-11	8.471096e-10
	0.5	8.807574e-07	5.754661e-02	4.555180e-07	7.544354e-02
	0.3	4.199235e-08	4.738905e-03	6.087159e-08	7.269472e-03
DGSE(Tet)	0.2	3.710406e-09	5.450330e-04	1.445380e-08	1.015404e-03
	0.1	5.841698e-11	1.044808e-05	3.801149e-09	2.872153e-05
	0.05	5.358965e-12	1.729992e-07	3.124237e-09	6.760630e-07
	0.025	7.785222e-12	2.753365e-09	3.298136e-09	1.895101e-08

Antonietti, P. F., Ayuso de Dios, B., Mazzieri, I., & Quarteroni, A., 2016a. Stability analysis of discontinuous Galerkin approximations to the elastodynamics problem, *Journal of Scientific Computing*, **68**(1), 143–170.

Antonietti, P. F., Ferroni, A., Mazzieri, I., & Quarteroni, A., 2016b. Convergence and stability analysis of the $hp-$version of the discontinuous Galerkin approximation of the elastodynamics equation, in *Proceedings of ICOSAHOM-2016*, Accepted for publication.

Antonietti, P. F., Marcati, C., Mazzieri, I., & Quarteroni, A., 2016c. High order discontinuous Galerkin methods on simplicial elements for the elastodynamics equation, *Numerical Algorithms*, **71**(1), 181–206.

Antonietti, P. F., Ferroni, A., Mazzieri, I., Paolucci, R., Quarteroni, A., Smerzini, C., & Stupazzini, M., 2017.

Table A3. Dispersion errors $|e_P|$ and $|e_S|$ versus δ, for $\theta = \varphi = \pi/4$ and $N = 4$.

		$r = 5$	$r = 5$	$r = 10$	$r = 10$
Scheme	δ	$\|e_P\|$	$\|e_S\|$	$\|e_P\|$	$\|e_S\|$
	0.5	2.243895e-11	2.158327e-06	1.427637e-13	3.687616e-06
	0.3	3.554774e-13	7.807056e-08	3.623139e-13	1.749918e-07
SE(Hex)	0.2	9.603958e-14	4.103992e-09	1.069703e-13	1.191819e-08
	0.1	2.352562e-14	1.970982e-11	1.784545e-13	7.705525e-11
	0.05	1.931386e-14	1.010776e-12	2.510300e-13	1.963246e-12
	0.025	2.100006e-14	4.776431e-12	1.823001e-13	3.218457e-12
	0.5	2.684473e-09	4.604364e-03	9.906742e-12	6.286153e-03
	0.3	4.572120e-11	1.124038e-04	1.720866e-13	1.619501e-04
SE(Tet)	0.2	1.795009e-12	4.659543e-06	1.911209e-14	6.567256e-06
	0.1	1.843133e-14	1.868424e-08	4.329871e-14	2.671163e-08
	0.05	4.596752e-14	7.341661e-11	1.756390e-13	1.060585e-10
	0.025	1.448151e-13	5.878777e-15	6.452692e-14	1.534441e-12
	0.5	2.358614e-11	2.069003e-06	5.517419e-09	2.046152e-06
	0.3	8.066900e-14	7.348344e-08	7.429552e-10	2.945856e-07
DGSE(Hex)	0.2	1.087382e-13	3.810877e-09	1.469110e-10	1.364408e-07
	0.1	3.604002e-13	2.033636e-11	1.363722e-11	1.461701e-08
	0.05	9.417545e-14	6.879545e-12	4.368198e-12	1.065253e-09
	0.025	2.884016e-13	1.229953e-12	3.463097e-12	8.824582e-11
	0.5	2.590493e-09	4.450872e-03	3.808418e-08	6.211804e-03
	0.3	4.401909e-11	1.080323e-04	5.004619e-09	1.580912e-04
DGSE(Tet)	0.2	1.548143e-12	4.478117e-06	9.918164e-10	6.065962e-06
	0.1	5.819818e-13	1.795117e-08	6.594085e-11	8.622549e-08
	0.05	2.079526e-13	7.134795e-11	6.103458e-12	1.566411e-09
	0.025	3.749187e-13	5.018842e-11	1.916163e-12	3.464867e-11

Numerical modeling of seismic waves by Discontinuous Spectral Element methods, *MOX Report*, (9/2017).

Arnold, D. N., 1982. An interior penalty finite element method with discontinuous elements, *SIAM Journal on Numerical Analysis*, **19**(4), 742–760.

Arnold, D. N., Brezzi, F., Cockburn, B., & Marini, L. D., 2002. Unified analysis of discontinuous Galerkin methods for elliptic problems, *SIAM Journal on Numerical Analysis*, **39**(5), 1749–1779.

Canuto, C., Hussaini, M., Quarteroni, A., & Zang, T., 2006. *Spectral methods: Fundamentals in single domains*, Springer, Berlin.

Chaljub, E. & Valette, B., 2004. Spectral element modelling of three-dimensional wave propagation in a self-

gravitating earth with an arbitrarily stratified outer core, *Geophysical Journal International*, **158**(1), 131–141.

Chaljub, E., Capdeville, Y., & Vilotte, J.-P., 2003. Solving elastodynamics in a fluid–solid heterogeneous sphere: a parallel spectral element approximation on non-conforming grids, *Journal of Computational Physics*, **187**(2), 457 – 491.

Chaljub, E., Komatitsch, D., Vilotte, J.-P., Capdeville, Y., Valette, B., & Festa, G., 2007. Spectral-element analysis in seismology, *Advances in Geophysics*, **48**, 365–419.

Chaljub, E., Moczo, P., Tsuno, S., Bard, P.-Y., Kristek, J., Käser, M., Stupazzini, M., & Kristekova, M., 2010. Quantitative comparison of four numerical predictions of 3d ground motion in the Grenoble valley, France, *Bulletin of the Seismological Society of America*, **100**(4), 1427–1455.

Cohen, G., 2002. *Higher-Order Numerical Methods for Transient Wave Equations*, Springer.

De Basabe, J. D. & Sen, M. K., 2007. Grid dispersion and stability criteria of some common finite-element methods for acoustic and elastic wave equations, *Geophysics*, **72**(6), T81–T95.

De Basabe, J. D. & Sen, M. K., 2010. Stability of the high-order finite elements for acoustic or elastic wave propagation with high-order time stepping, *Geophysical Journal International*, **181**(1), 577–590.

De Basabe, J. D., Sen, M. K., & Wheeler, M. F., 2008. The interior penalty discontinuous Galerkin method for elastic wave propagation: grid dispersion, *Geophysical Journal International*, **175**(1), 83–93.

Dumbser, M. & Käser, M., 2006. An arbitrary high-order discontinuous Galerkin method for elastic waves on unstructured meshes – II. The three-dimensional isotropic case, *Geophysical Journal International*, **167**(1), 319–336.

Epshteyn, Y. & Rivière, B., 2007. Estimation of penalty parameters for symmetric interior penalty Galerkin methods, *Journal of Computational and Applied Mathematics*, **206**(2), 843–872.

Eringen, A. & Şuhubi, E., 1975. *Elastodynamics: Linear theory*, Elastodynamics, Academic Press.

Faccioli, E., Maggio, F., Paolucci, R., & Quarteroni, A., 1997. 2d and 3d elastic wave propagation by a pseudo-spectral domain decomposition method, *Journal of seismology*, **1**(3), 237–251.

Fichtner, A., 2010. *Full Seismic Waveform Modelling and Inversion*, Springer-Verlag, Heidelberg.

Fichtner, A., Igel, H., Bunge, H.-P., & Kennett, B. L. N., 2009. Simulation and inversion of seismic wave propagation on continental scales based on a spectral-element method, *Journal of Numerical Analysis, Industrial and Applied Mathematics*, **4**(1-2), 11–22.

Karniadakis, G. & Sherwin, S., 2005. *Spectral/hp element methods for computational fluid dynamics*, Oxford University Press, 2nd edn.

Käser, M. & Dumbser, M., 2006. An arbitrary high-order discontinuous Galerkin method for elastic waves on unstructured meshes – I: The two-dimensional isotropic case with external source terms, *Geophysical Journal International*, **166**(2), 855–877.

Komatitsch, D. & Tromp, J., 1999. Introduction to the spectral element method for three-dimensional seismic wave propagation, *Geophysical Journal International*, **139**(3), 806–822.

Komatitsch, D. & Tromp, J., 2002. Spectral-element simulations of global seismic wave propagation–II. Three-dimensional models, oceans, rotation and self-gravitation, *Geophysical Journal International*, **150**(1),

303.

Liu, T., Sen, M. K., Hu, T., De Basabe, J. D., & Li, L., 2012. Dispersion analysis of the spectral element method using a triangular mesh, *Wave Motion*, **49**(4), 474–483.

Mazzieri, I. & Rapetti, F., 2012. Dispersion analysis of triangle-based spectral element methods for elastic wave propagation, *Numerical Algorithms*, **60**(4), 631–650.

Mazzieri, I., Stupazzini, M., Guidotti, R., & Smerzini, C., 2013. Speed: Spectral elements in elastodynamics with discontinuous Galerkin: a non-conforming approach for 3d multi-scale problems, *International Journal for Numerical Methods in Engineering*, **95**(12), 991–1010.

Mercerat, E., Vilotte, J., & Sánchez-Sesma, F., 2006. Triangular spectral element simulation of two-dimensional elastic wave propagation using unstructured triangular grids, *Geophysical Journal International*, **166**(2), 679–698.

Mercerat, E. D. & Glinsky, N., 2015. A nodal high-order discontinuous Galerkin method for elastic wave propagation in arbitrary heterogeneous media, *Geophysical Journal International*, **201**(2), 1101–1118.

Moczo, P., Kristek, J., & Gális, M., 2014. *The Finite-Difference Modelling of Earthquake Motions: Waves and Ruptures*, Cambridge University Press.

Mulder, W. A., Zhebel, E., & Minisini, S., 2014. Time-stepping stability of continuous and discontinuous finite-element methods for 3-d wave propagation, *Geophysical Journal International*, **196**(2), 1123–1133.

Pasquetti, R. & Rapetti, F., 2006. Spectral element methods on unstructured meshes: comparisons and recent advances, *Journal of Scientific Computing*.

Patera, A. T., 1984. A spectral element method for fluid dynamics: laminar flow in a channel expansion, *Journal of Computational Physics*, **54**(3), 468–488.

Peter, D., Komatitsch, D., Luo, Y., Martin, R., Le Goff, N., Casarotti, E., Le Loher, P., Magnoni, F., Liu, Q., Blitz, C., Nissen-Meyer, T., Basini, P., & Tromp, J., 2011. Forward and adjoint simulations of seismic wave propagation on fully unstructured hexahedral meshes, *Geophysical Journal International*, **186**(2), 721–739.

Quarteroni, A. & Valli, A., 2008. *Numerical approximation of partial differential equations*, vol. 23, Springer Science & Business Media.

Rivière, B. & Wheeler, M. F., 2003. Discontinuous finite element methods for acoustic and elastic wave problems, *Contemporary Mathematics*, **329**, 271–282.

Rivière, B., Shaw, S., & Whiteman, J., 2007. Discontinuous Galerkin finite element methods for dynamic linear solid viscoelasticity problems, *Numerical Methods for Partial Differential Equations*, **23**(5), 1149–1166.

Seriani, G. & Oliveira, S., 2008. Dispersion analysis of spectral element methods for elastic wave propagation, *Wave Motion*, **45**(6), 729–744.

Seriani, G., Priolo, E., & Pregarz, A., 1995. Modelling waves in anisotropic media by a spectral element method, in *Proceedings of the third international conference on mathematical and numerical aspects of wave propagation*, pp. 289–298, SIAM.

Sherwin, S. J. & Karniadakis, G. E., 1995. A new triangular and tetrahedral basis for high-order (hp) finite element methods, *International Journal for Numerical Methods in Engineering*, **38**(22), 3775–3802.

Stupazzini, M., Paolucci, R., & Igel, H., 2009. Near-fault earthquake ground-motion simulation in the Grenoble valley by a high-performance spectral element code, *Bulletin of the Seismological Society of America*, **99**(1), 286–301.

Warburton, T., 2006. An explicit construction of interpolation nodes on the simplex, *Journal of Engineering Mathematics*, **56**(3), 247–262.

Wheeler, M. F., 1978. An elliptic collocation-finite element method with interior penalties, *SIAM Journal on Numerical Analysis*, **15**(1), 152–161.

Zyserman, F. I. & Gauzellino, P. M., 2005. Dispersion analysis of a nonconforming finite element method for the three-dimensional scalar and elastic wave equations, *Finite elements in Analysis and Design*, **41**(13), 1309–1326.